2010

A genetic algorithm approach in interface and surface structure optimization

Jian Zhang
Iowa State University

A genetic algorithm approach in interface and surface structure optimization

by

Jian Zhang

A dissertation submitted to the graduate faculty

in partial fulfillment of the requirements for the degree of

DOCTOR OF PHILOSOPHY

Major: Condensed Matter Physics

Program of Study Committee:
Kai-Ming Ho, Major Professor
Ruslan Prozorov
Edward Yu
Jianwei Qiu
Jim Evans

Iowa State University

Ames, Iowa

2010

TABLE OF CONTENTS

LIST OF TABLES

LIST OF FIGURES

ACKNOWLEDGEMENTS

I would like to take this opportunity to express my thanks to Dr. Ho for his help and support. His keen insights on the research subjects and patient guidance on the my graduate research enable me to finish my graduate education.

ABSTRACT

The thesis is divided into two parts.

In the first part a global optimization method is developed for the interface and surface structures optimization. Two prototype systems are chosen to be studied. One is Si[001] symmetric tilted grain boundaries and the other is Ag/Au induced Si(111) surface. It is found that Genetic Algorithm is very efficient in finding lowest energy structures in both cases. Not only existing structures in the experiments can be reproduced, but also many new structures can be predicted using Genetic Algorithm. Thus it is shown that Genetic Algorithm is a extremely powerful tool for the material structures predictions. The second part of the thesis is devoted to the explanation of an experimental observation of thermal radiation from three-dimensional tungsten photonic crystal structures. The experimental results seems astounding and confusing, yet the theoretical models in the paper revealed the physics insight behind the phenomena and can well reproduced the experimental results.

CHAPTER 1. Introduction to genetic algorithm

Genetic Algorithms (GAs) are adaptive heuristic search algorithm based on the evolutionary ideas of natural selection and genetics.[1-6] As such they represent an intelligent exploitation of a random search used to solve optimization problems. They exploit historical information usually produced from parent generations to direct the search into the region of better performance within the search space in the next generation. The basic techniques of the GAs are designed to simulate processes in natural systems necessary for evolution, specially those follow the principles first laid down by Charles Darwin of "survival of the fittest". [1-3]Since in nature, competition among individuals for scanty resources results in the fittest individuals dominating over the weaker ones.

There a number of optimization methods used in scientific and engineering applications, including some deterministic methods like Branch and Bound methods and stochastic ones like simulated annealing.[2] The reason to choose GA is that it is better than conventional search methods in that it is more robust and usually faster in exploring the search space. In searching a large state-space, multi-modal state-space, or n-dimensional surface, a genetic algorithm may offer significant benefits over more typical search of optimization techniques as GA relies little on the input information and GA has exceptional abilities to bypass the local minimum or maximum in the path of global optimization.

GAs simulate the survival of the fittest among individuals over consecutive generation for solving a problem. Each generation consists of a population of character strings that are analogous to the chromosome that we see in our DNA. Each individual represents a point in a search space and a possible solution. The individuals in the population are then made to go through a process of evolution. A certain fitness criterion is often used to evaluate the fitness

of the solutions and the strongest solutions will survive to participate in the following evolution process.

John Holland, from the University of Michigan began his work on genetic algorithms at the beginning of the 60s. A first achievement was the publication of Adaptation in Natural and Artificial System in 1975.[4] From then on more and more complicated optimization problems are being solved using GA in a huge number of areas such as biology, engineering, finance or even business. In recent years GA has been applied to optimize complicated material structures problems. All possible atomic positions in the structure constitute a large search space which imposes big challenges for traditional search algorithms. Genetic Algorithm is proven to be efficient for many of those problems. In the following chapters we will discuss the use of GA in optimizing interface and surface structures. We will present in chapter 2 a prototype interface structure Si[001] Symmetric Tilted Grain Boundaries and in chapter 3 we will present another very important surface structure in Ag/Au induced Si(111) surface reconstructions.

CHAPTER 2. Finding low energy structure of Si[001] symmetric tilted grain boundaries with a genetic algorithm

1 Introduction

We have developed a global structure optimization method, Genetic Algorithm, for fast and efficient prediction of grain boundary structures. Using this method we predict the most stable structures for Si[001] symmetric tilted grain boundaries with multiple tilted angles and a number of low-energy metastable structures for each angle. Existing structure models are well reproduced and many new structures are also found. A developed Environmental-Dependent tight binding potential model for Si is used for evaluating the energies of the selected structures and found to be in very good agreement with the first principle calculation result. Thus it can be an extremely useful tool for Si grain boundary calculation as the system size becomes big.

Grain boundaries (GB) play an important role in microstructure stability, mechanical behavior, and transport properties of many polycrystalline materials. Grain boundaries are also considered to be the major defects affecting the performance of many microelectronic materials and devices, such as micromechanical materials, nanocrystalline materials, and solar energy application devices.[7-10] Therefore understanding the structures of grain boundaries at the atomic level is highly desirable. However, structural complexity of grain boundaries makes both experimental and theoretical studies difficult. Although the experimental tools like high resolution transmission electron microscopy (HRTEM) are widely used in studying grain boundaries in materials, the experimental resolution necessary to examine the detailed atomic structure of grain boundary is still difficult to achieve. On the other hand, many possible structures for a given grain boundary also makes theoretical study complicated. [10-16]The relatively large system size (hundreds to thousands atoms) makes first principle calculations

very costly. Meanwhile, many classical potentials, which are fast and useful for calculating system with large size, need to be checked for their accuracy.[10-16]

The atomic structures of grain boundaries in Si have received lots of interest both experimentally and theoretically.[10-16] Ball and stick modeling is first used to deduce plausible reconstructions based on the hypothesis that the coordination in grain boundary structures preserve that of crystals as far as possible.[7-9] Further modeling using molecular dynamics, Monte Carlo annealing is also used to explore possible GB structures. [16-18]Among those studies Si[001] Symmetric Tilted Grain Boundaries have attracted the most interest. The energies of symmetrical tilted GB in Si have been characterized using lots of calculation methods including first principles density functional theory (DFT) calculations, semiempirical tight binding methods (TB), analytical bond-order potential and other classical potentials. [10-16]

In this paper we will use an efficient global optimization method, genetic algorithm (GA) to generate the structure of grain boundary. Genetic algorithm is an optimization strategy inspired by the Darwinian evolution process. The GA operation is analogous to the process of natural selection of the fittest offsprings. At the end of each GA run, the fittest structures are remaining in the GA pool. GA has already enjoyed huge successes in determining the structures of various dimensions including atomic clusters, crystal structures, nanowires and surface structures. [19-24]

There are two clear advantages of Genetic Algorithm over the other methods:

(1) Genetic Algorithm has an effective way of overcoming energy barriers by its mating algorithm. When designed properly, it can explore extensively into the whole energy landscape without trapping into the local minimum for too long. On the other hand, other methods like molecular dynamics or Monte Carlo approach are much easier to remain into the local minimum without moving out due to the high energy barriers. So the efficiency in GA can be much better than other methods especially when the overall energy landscape has many local minimums and the energy barriers are high for those minimums.

(2) Usually Genetic Algorithm requires little information on the initial structure. It does not make assumptions on the shape or topology of the energy landscape. The first generation

of structures in GA are almost always produced randomly without starting from certain initial structures. While in other methods reasonably good starting structures are often needed in order to make transitions to the desired structures.

This paper is arranged as follows. In section 2, the GA method used in our grain boundary structure optimization will be discussed in details. The grain boundary structures obtained from our GA search are presented in section 3. The energies of the grain boundary are further discussed in section 4 followed by the summary in section 5.

2 The genetic algorithm method

Here we investigated the structures and energies of Si[001] symmetrical tilted GBs using the Genetic Algorithm approach. The symmetrical tilted Si[001] GB can be constructed by rotating the two Si grains in the opposite direction by the same angle around the (001) rotation axis and then matching the two grains together. [18]Thus in the direction of the boundary plane the GB will show periodic structures. We model the GB using a simulation block with periodic conditions in the x and y directions parallel to the boundary plane. In the perpendicular direction z, the grains are terminated at free surfaces. The geometry and dimensions of the computational cells are shown in Fig. 2.1.

Atomic positions in the cell are generated from geometrical coincident site lattice (CSL) construction. In this geometry, the rigid body translations (RBT's) are free to occur if they lead to more energetically favorable structures. The thickness of the grains is large enough to exclude interactions between the GB and surfaces. This is also verified by repeating selected calculations with different thicknesses and checking that the results are nearly the same. In this paper the thickness is chosen to be ten times of the period in the x direction.

A special designed Genetic Algorithm is used to produce the structures of grain boundaries. As the atomic structure of grain boundaries can be seen as a reconstruction of the interface atoms. We first choose the interface area between the two grains, which we call the GA cell, shown in Fig. 2.1. The GA operations will be run on the atoms inside the GA cell while atoms outside the GA cell are allowed to relax to a local minimum of the potential energy after each

GA operation.

The optimization procedure developed here is based on the idea of evolutionary approach in which the number of a generation (pool of models for the interface) is generated with the goal of producing the best specimens, i.e. lowest energy reconstructions. We can divide the algorithm in the following procedures:

The first procedure is initial pool construction, which we call "Generation zero". In the beginning we will have a pool of p different structures obtained by randomizing the positions of the atoms inside the GA cell, and by subsequently relaxing the simulation cell through molecular static relaxation.

The second is mating, which is the evolution from one generation to the next one. We can generate an offspring structure from two randomly picked structures in the pool of current generation through a mating operation: $\mathcal{O}$:(A,$B \longrightarrow C$). As in Fig. 2.2 two parent structures A and B are randomly selected from the pool and the two GA cell are separated and sectioned by an arbitrary plane perpendicular to the surface of the cells. The new GA cell is created by combining the part of A that lies to the left of the cutting plane and the part of B lying to the right of that plane. Then the new GA cell is combined with the rest parts (either from A or B) to form a new child structure C. Structure C is then further relaxed to the nearest local minimum with conjugate gradient minimization. Two versions of the genetic algorithm could be developed. In the first version the number of atoms inside the GA cell is kept constant by automatically rejecting the child structures that have different number of atoms from their parents. In the second one the restriction is not enforced thus it is possible to have a different number of atoms in the child than its parent. Here we choose the second version as it allows us to do a wider range of search over more different structures.In each generation, a number of m mating operations are performed.

The third procedure is updating the pool. From mating procedure above we have m children structures. They are relaxed and considered for the possible inclusion in the pool based on their grain boundary energy. If there exist at least one candidate in the pool that has a higher grain boundary energy than that of the child considered, then the child structure is included in

the pool. Upon inclusion of the child, the structure with the highest grain boundary energy is discarded in order to preserve the total population p. To avoid crowding the pool with identical metastable configurations, we retain a new structure only if its energy differs by more than δ when compared to the energy of any of the current member p of the pool. We also consider a criterion based on atomic displacements to account for the (theoretically possible) situation in which two structures have equal energy but different topologies: two structures are considered structurally different if the relative displacement of at least one pair of corresponding atoms is greater than ϵ. Relevant values for the parameters of the genetic genetic algorithms are p=30, m=15, d=5A, δ=10^{-5}, and $\epsilon = 0.2A$

The fourth procedure is to repeat the mating process in a new generation and update the pool after m mating operations are done. We can keep repeating for hundreds to thousands of generations until the desired structures are found in the pool.

3 Structures generated by the genetic algorithm

A Symmetrical Si[001] tilt grain boundary can be described as a GB with median plane (110) or (100) and a rotation angle with the range from 0° to 90°.[21] We searched for the structures of Si GB's at 18 disorientation angles with GA using the classical stillinger-Weber potential. In each GA run, after a number of generations, final structures can be obtained from the GA pools. In each pool we can find the ground state structure, which is the structure with the lowest energy calculated using the Stillinger-Weber potential together with many higher energy metastable structures. These lowest-energy structures are in agreement with previous theoretical and experimental results while they are produced by GA with much higher efficiency. As a result of the way of GA is designed, only one GA run is needed to obtained all the lower-energy structures in the final pool. For example, in Figs.2.4-2.7 we show the GB structures of four different orientation angles from 0° to 90° respectively. In these figures, we show not only the lowest-energy structures, but also some lower-energy metastable structures. After a careful look at the results we can see that the structural unit model(SUM) is generally a good description of the structures we have found. The structural unit model describes GB's in terms

of structural units (SU's) consisting of either the perfect crystal structure or dislocation cores with the associated Burgers vectors.[22,23] The majority of Si[001] symmetrical tilted GB's in the entire range of disorientation can be constructed from three characteristic structural units as shown in Fig. 2.3: unit A, a pure edge dislocation core, with a burgers vector $b = \frac{1}{2}a_0[110]$, where a_0 is the lattice constant of the perfect crystal.; unit B, the core of a 45° mixed dislocation, with burgers vector inclined at 45° to the rotation axis. This mixed dislocation core has a screw component, which is parallel to the rotation axis ; unit C, the unit of a perfect crystal. Also we can see that there are generally two basic ways how those structural units are connected to form the grain boundary: the straight way or the zigzag way. The sequence of the structural units arranged and the way they are connected will have an impact on the GB energies they have, which we will illustrate in the following examples:

In Fig. 2.4 we show a typical example of the small angle grain boundary with tilted angle 16.26°. For ground state structures with the small angles the grain boundary structures can often be seen as rows of parallel pure edge dislocations (unit A), which is a pentagonal-triangular pattern shared with a same edge, separated by a series of good crystal units (unit C). In this case the structure Fig.4 (a) has two dislocation core structures separated by five crystal structure units between them, which gives a $CCCCCACCCCCA$ arrangement in the GB area. This structure also has a mirror like symmetry across the boundary plane. The structures shown in Fig. 2.4(b), Fig. 2.4(c), Fig. 2.4(d) are some of the higher energy structures in the pool. Among b, c, d only structure Fig. 2.4(c) preserve the mirror like symmetry across the GB plane. Structure Fig. 2.4(c) has the same set of units as structure Fig. 2.4(a). However it has a different unit arrangement as $CCCACCCCCCCA$, which results in higher GB energy. Structure Fig. 2.4(b) has similar units arrangement but the dislocation cores are shifted apart in the (110) direction, which causes a higher energy. Structure Fig. 2.4(d) can be seen as formed by the addition of extra dislocations introduced to the Fig. 2.4(a) structure, which will also raise the GB energy. Besides those four structures, there are also numerous new structures in this rotation angle in the GA pool, which shows the multiplicity of GB structures in a given rotation angle. This multiplicity, which demonstrates the complexity of GB material, is also

found in experiments.[25-26]

It is not surprising that the small angle GB will have lots of units of perfect crystal lattice as the small angle will likely to add a small perturbation to the perfect crystal like structure and introduce some dislocation cores. [15]The majority of the crystal like units would like to be preserved. However, when the rotation angle becomes bigger, the number of crystal units will shrink and more dislocation core structures will be introduced . In Fig. 2.5 the rotation angle is increased to 36.87° .Structure Fig. 2.5(a) has a structure unit arrangement as $ACAC$ in one period, which has two unit A dislocation cores separated by a single crystal unit C, the burgers vector for the dislocations is the same as Fig. 2.5(a) structure while the number of C units are greatly decreased due to the larger orientation angle. Meanwhile the periodicity in the grain boundary plane becomes much shorter compared to the low angle grain boundary structures in Fig. 2.4. In Fig. 2.5 other structures all have more complicated arrangement of dislocations cores and forms zigzag boundaries. Only structure Fig. 2.4(a) has a straight boundary plane and its energy is the lowest.

In Fig. 2.6 when the rotation angle is further increased to 53.15°, (130) boundary is formed and the period in the boundary plane is even shorter. Structure Fig. 2.6(b) has two dislocation core units A connected together and crystal unit C is absent, making the structure units arrangement as simply AA. What is interesting is that in this case it is not the lowest energy structures compared to the Fig.6(a) structure, which is a zigzag structure of two A units. We can find that other metastable structures Fig. 2.6(c),Fig. 2.6(d),Fig. 2.6(e),and Fig. 2.6(f) have more complicated dislocations connected together and structure Fig. 2.6(e) cannot be described by the three basic structural units A, B, C defined above as the triangular and pentagonal rings are separated by a crystal unit. This might suggest that when the rotation angle becomes big, the matching of the two grains becomes flexible compared to the low angle case and more exotic structures may appear, which is further illustrated in Fig. 2.7.

In Fig. 2.7 the rotation angle is 67.38°, making the GB a high angle one. Structures in this rotation angle have been studied extensively both experimentally and theoretically in the previous work. [18, 26-27]A variety of structures exist in this angle and interestingly,

the structure with the lowest energy is the one that has the most dislocation dipole content. [18]Here using GA we have successfully reproduced all the structures reported in the literature and we also get some new structures constructing with different units. The structures in Fig. 2.7 are named according to the literature.[18] From the structural unit viewpoint, most of the (150) structures can be constructed using a mixed dislocation core, B with crystal units C. For example, Fig. 2.7 ($S20$) and Fig. 2.7 ($S11$) have straight arrangement $BBCC$ and $BCBC$ respectively while Fig. 2.7 ($Z20$) and Fig. 2.7 ($Z11$) have zigzag arrangement $BBCC$ and $BCBC$ respectively. There are also exceptions which the atomic structures cannot be explained by the basic units arrangement. Fig.2.7($I0$, Fig.2.7($New1$) and Fig.2.7($New2$) all have very rare six member rings that are not found in GBs of other rotation angles. Fig.2.7($New3$) are similar to the Fig.2.7($I0$) but with a larger outward shift between the two grains, which makes an eight member ring structure from the six ring structure. The multiplicity of these structures might be attributed to the fact that high angle grain boundary gives more flexibility for atoms reconstructing in the GB area. Overall this high angle grain boundary (150) has more dislocation cores than the low angle ones. These structures have similar energies and that may be the reason why multiple structures can be observed in this angle experimentally with HRTEM and Z-contrast electron technique.[27]

4 Grain boundary energy calculations

The structures obtained from the GA search are then used as starting points for first-principles and tight binding calculations of the GB energies. This is done in the following way: A fully periodic system can be made by matching the two identical boundaries in the z direction together so that it will have periodicity in direction perpendicular to the boundary plane in addition to the periodicity in the x-y plane from the GA generated structure. This method is similar to that used in Ref[12]. In the new structure the two grain boundaries, which have opposite directions, are approximately 50 A apart, depending upon the details of the structures. The number of atoms range from 200 to over 1000 for all the structures we constructed. In these calculations, the dimension normal to the grain boundary is roughly 10 times larger than

the dimension along the boundaries, which are similar to the surface slab calculations. A set of four special k points is chosen to sample the two-dimensional rectangular Brillouin zone. All the atoms in the system are allowed to relax until the forces are less than $10mev/A$. The first-principles calculations are performed using the VASP code and tight-binding calculations are performed using the environment-dependent Si tight-binding potential developed by Wang et al.[28]. The grain boundary energy is defined as

$$E_{GB} = \frac{(E_{slab} - NE_{bulk})}{S_{GB}} \tag{2.1}$$

where N is the number of atoms in the structure, E_{bulk} is the bulk energy of silicon and S_{GB} is grain boundary area.

Since first principles calculations require lots of computational resources for large systems, a number of selected systems with shorter periods along the grain boundaries(Si[001](120) and Si[001](130)) are computed using ab initio techniques here. These are also the relatively high angle grain boundary structures that can exhibit multiple structures with similar energy. We also used environment-dependent tight-binding potential model for Si to test how well it produced the grain boundary energy.[28] This potential goes beyond the two center approximation by allowing the hopping terms to be modified by local atomic environment, which yields an improved transferability away from the bulk environment.

In Fig. 2.8 We show the GB energies of several Si[001](120) and Si[001](130) structures. Those energy values are obtained from ab initio calculations, Environment-Dependent Tight-Binding Potential and classical Stillinger-Weber potential. One striking observation is that result using tight-binding potential agrees very well with the first principle calculation result while the classical potential gives a significant deviation. In particular, the tight-binding result gives the correct energy ordering and reasonably good energy difference of the structures while the classical potential cannot. This suggests that the classical potential, which performs fast in calculation, is good to be used in the Genetic Algorithm search to explore all the possible structures with high efficiency. However, the TB model can be effectively used as a calculation tool for examining these grain boundary energies, even with large unit cells. It has also been shown previously that the environment-dependent Si tight binding potential also gives a good

description of the energies Si[100](150) grain boundary [18]. Since the ab initio calculation requires a lot of computer time and resources, the TB potential model for Si can be used as a more suitable way to identify structures and calculating energies.

In Fig.2.9 We show the lowest energies of GB in a given angle as a function of the total angles from both classical potential and tight binding calculations. It can be seen that some lower period structures like Si[100](120) and Si[100](130) have energies as the local minimums among the surrounding structures. Thus these structures, which have special angles and low periodicity, usually have the higher possibility of being observed in the experiment. In fact, faceting of the Grain Boundary can usually happen when the rotation angle of the GB is close to these special angles. Then faceting provides an efficient way of greatly reducing the GB energies.

5 Summary

We have developed a Genetic Algorithm to predict Si[001] symmetrical tilted grain boundary. This method is highly efficient and accurate for the grain boundary structure generation and reproduces all the structures both observed in experiments and deduced by the theoretical calculations. Almost all the GB structures can be expressed in the structural unit model except for a few high angle cases in which six and eight ring structures appear. Starting from the low angle grain boundary, as the disorientation angle between the grains becomes bigger, the number of perfect crystal unit in the grain boundary area will decrease and the connection between dislocation cores will become complex. The Environment-Dependent Tight-Binding Potential for Si is used to evaluate the energy of selected grain boundary structures and have a very good agreement with the first-principles calculation results. It provides us a useful tool for evaluating the energy orders of the structures and making corrections for the traditional classical potential results.

Besides the symmetrical tilted GB, more types of GBs including the twisted and asymmetrical ones can also be explored by the Genetic Algorithm in the similar way. This would be done in the later work. For Si GBs the Environment-Dependent Tight-Binding potential would

always be a valuable tool for the GB energy calculation due to its high transferability.

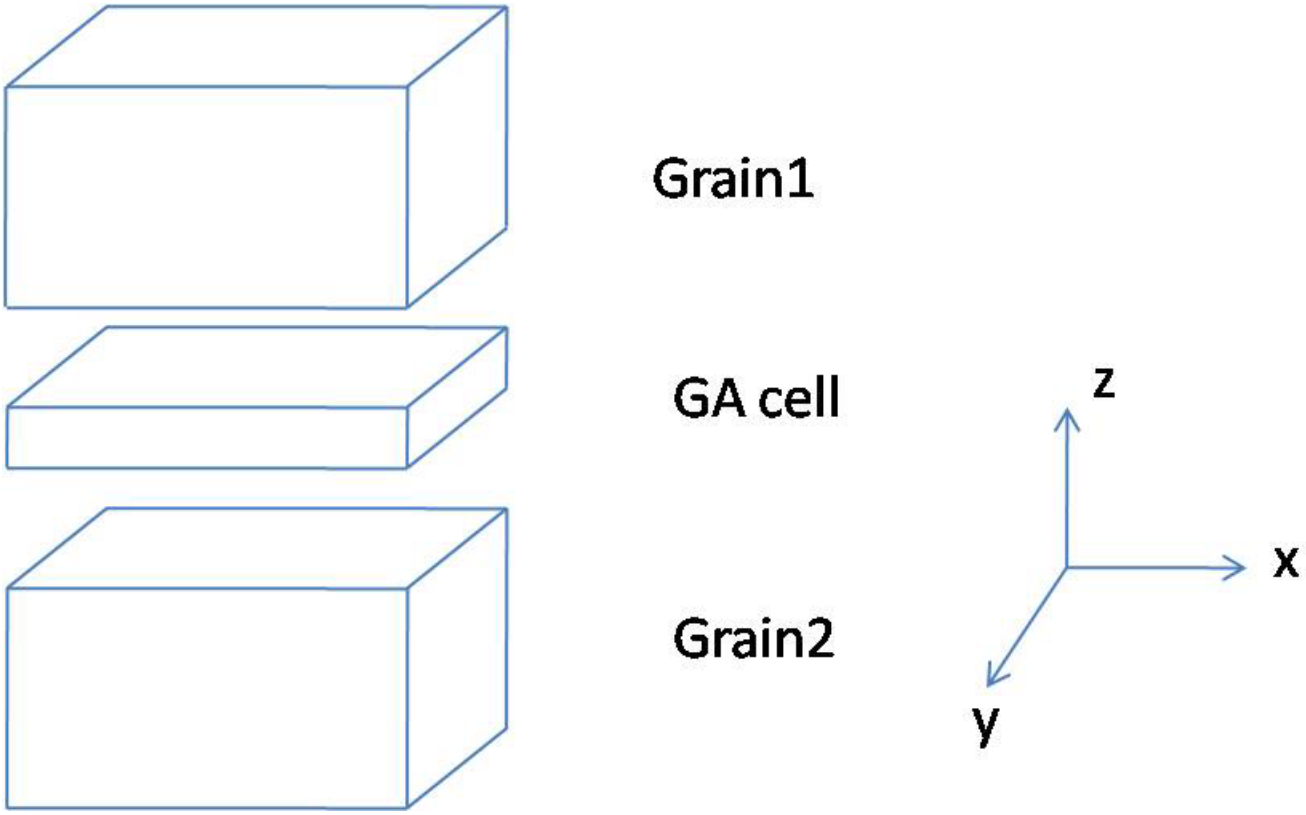

Figure 2.1 The computation cell for the GA search. x and y directions are periodic while z direction is terminated at free surfaces. The interface area between the two grains are called the GA cell.

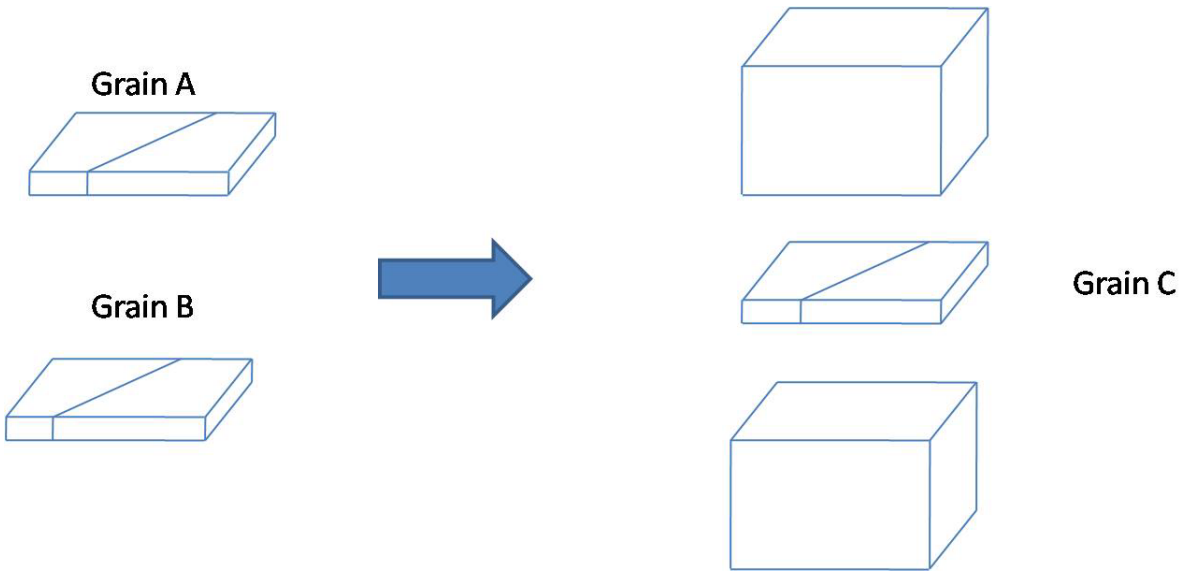

Figure 2.2 The mating operation $\mathcal{O}$:(A,B⟶C) From the two candidate structures A and B, which are separated by the same arbitrary plane oriented perpendicular to the surface. A new slab C is created by combining the part A that lies to the left of the cutting plane and the part of slab B which is laying to the left of the plane. C is placed between the two grains and the resulting structure is totally relaxed.

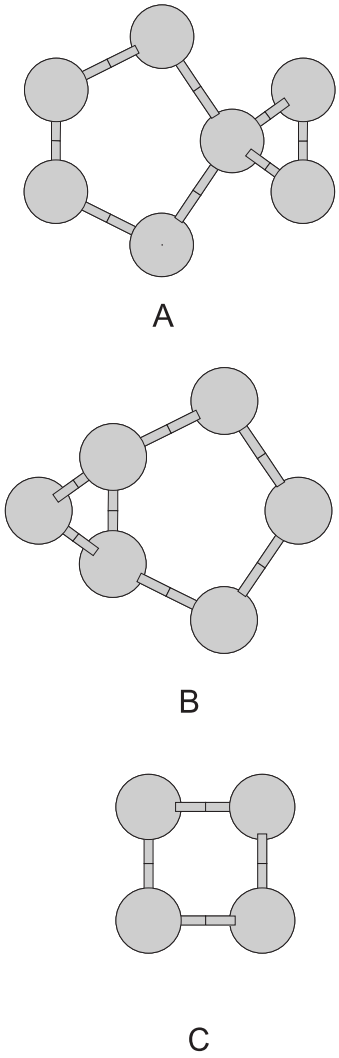

Figure 2.3 The structural Units(SU's) for the Si[001] symmetrical tilted grain boundaries. Three types of units are available: A is a core of pure edge dislocation, B is a mixed core dislocation with screw component and C is the unit of a perfect crystal structure.

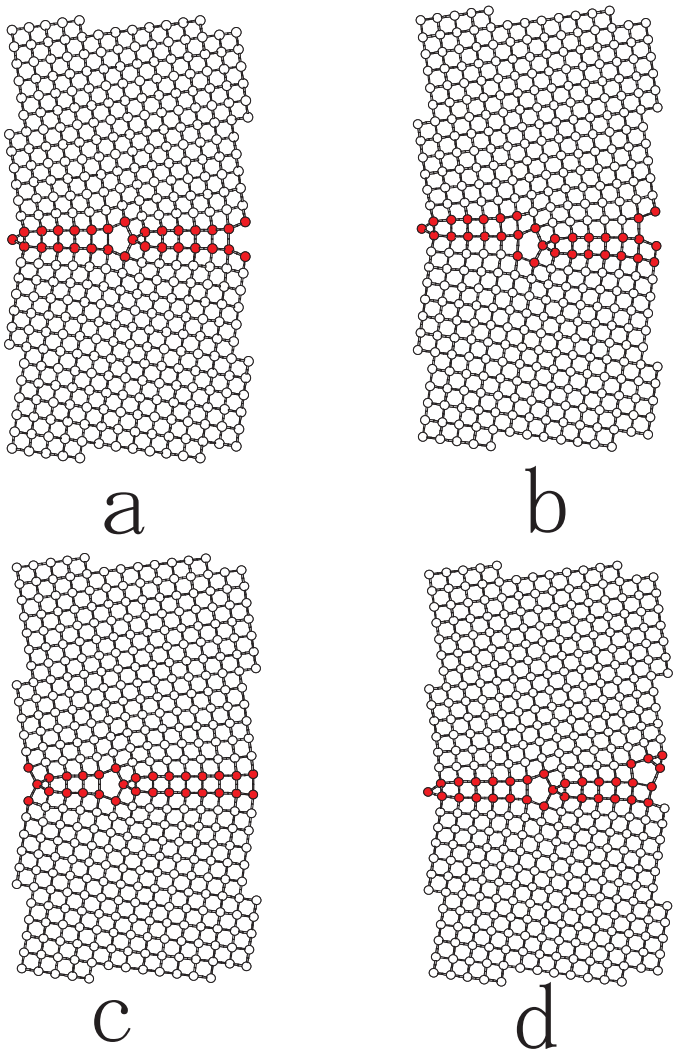

Figure 2.4 Atomic structures of $\Sigma = 25$ Si[001](340) GB, with rotation angle $\theta = 16.26\,^{\circ}$

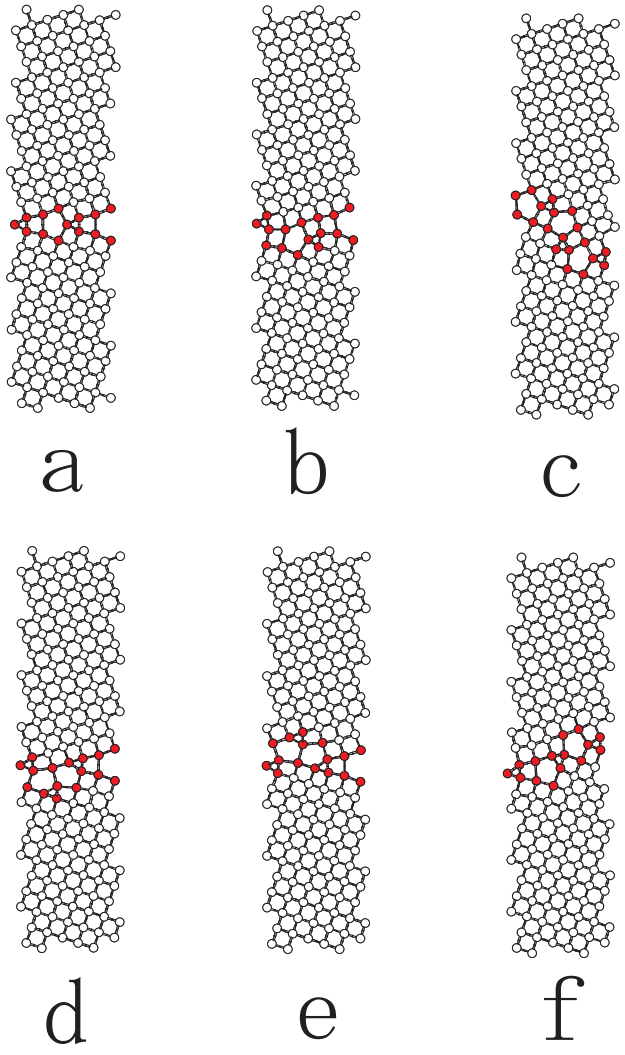

Figure 2.5 Atomic structures of $\Sigma = 5$ Si[001](120) GB, with rotation angle $\theta = 36.87\,^{\circ}$

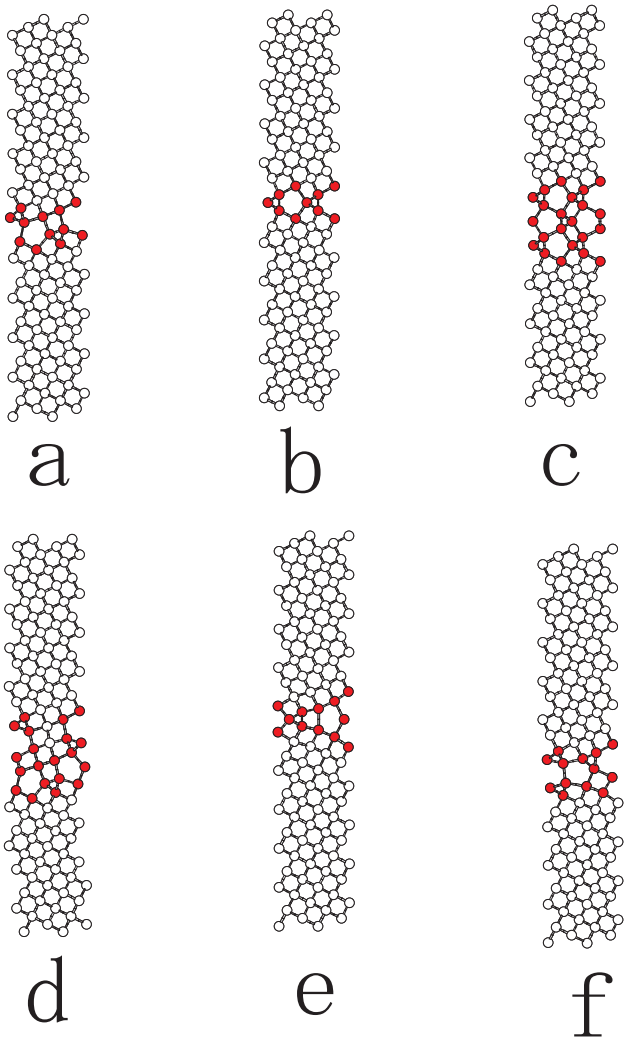

Figure 2.6 Atomic structures of $\Sigma = 5$ Si[001](130) GB, with rotation angle $\theta = 53.15\,^{\circ}$

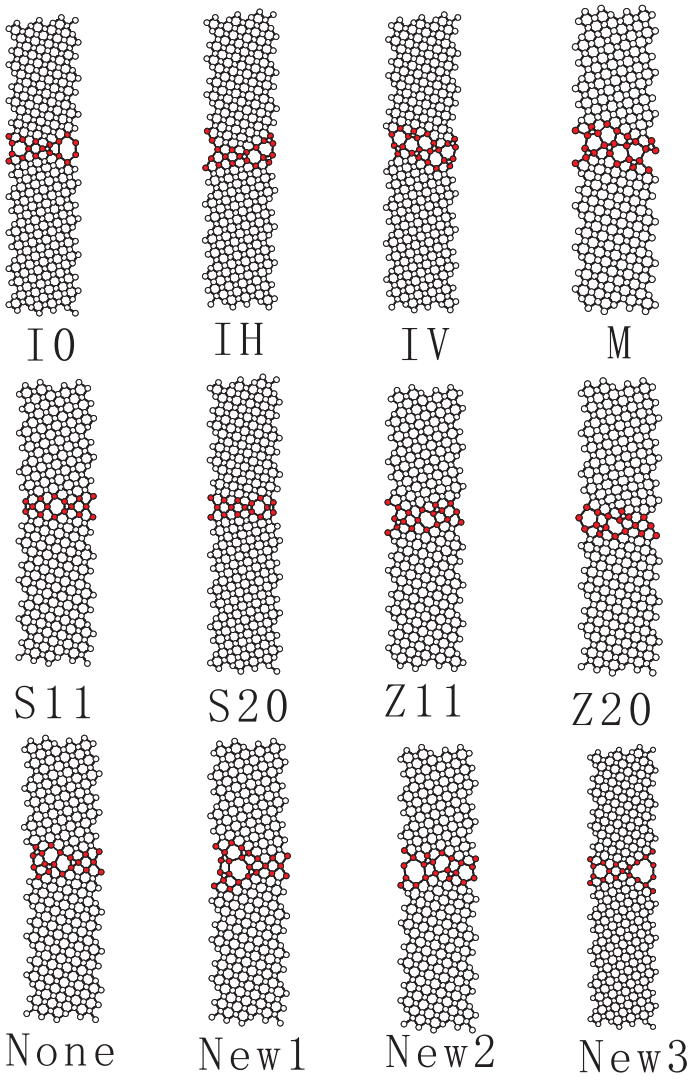

Figure 2.7 Atomic structures of $\Sigma = 13$ Si[001](150) GB, with rotation angle $\theta = 67.38^\circ$

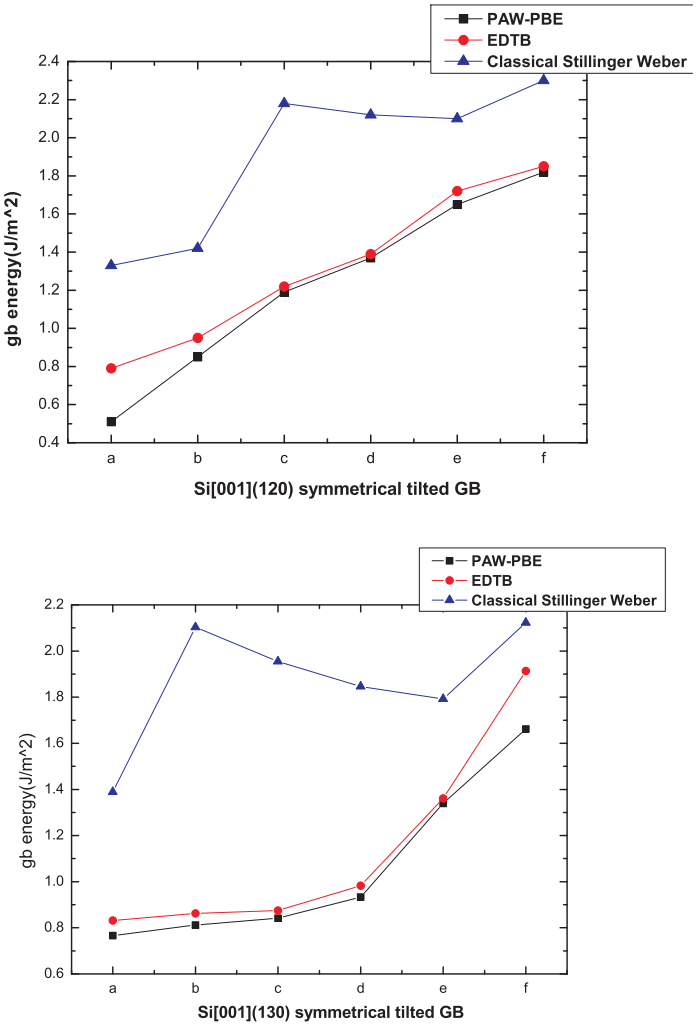

Figure 2.8 GB energies for Si[001](120) and Si[001](130) calculated in three different ways: DFT calculation,Environmental-Dependent Tight-Binding potential calculation and Classical Stillinger-Weber potential calculation.

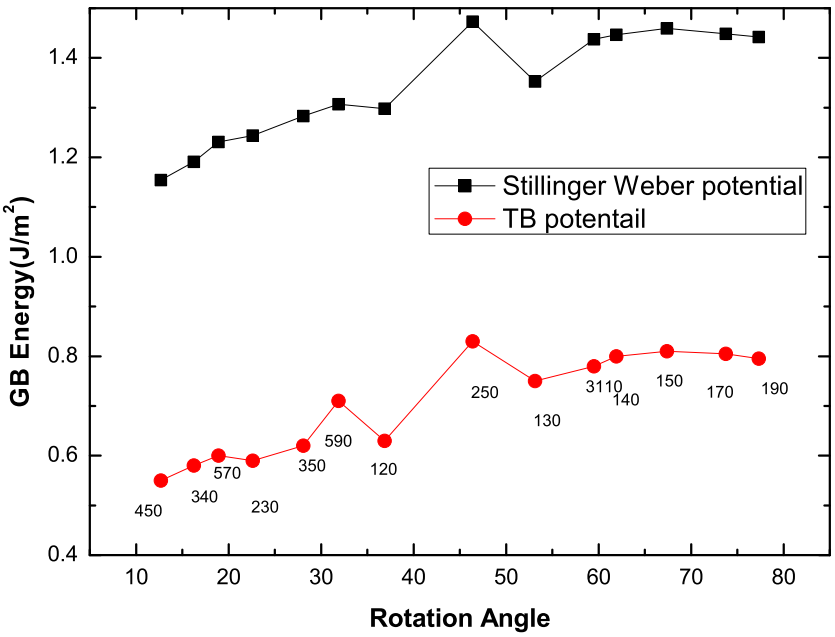

Figure 2.9 GB energies shown as a function of rotation angles.

CHAPTER 3. Structure of silver and gold induced silicon (111) surface reconstructions with a genetic algorithm

1 Introduction

The growth of metals on Si(111) surface has been the focus of many studies over the past several decades. One of the prototypical metal-semiconductor interfaces is the silver-silicon interface. Limited reaction or intermixing between two species reduces the complexity of interface structures between Ag and Si. However, there are several aspects of the Ag/Si(111) system that have remained unresolved. The detailed phase diagram presented by [29-32]. [29] shows that Si(111) surface under submonolayer Ag coverage the Si(111) surface exhibits $\sqrt{3} \times \sqrt{3}$, 3×1 and 5×2 phases. The atomic arrangements of $\sqrt{3} \times \sqrt{3}$ and 3×1 phases have been well studied[29- 38]. whereas there is no follow-up study after the first report of 5×2 phase presented by [23]. For Gold induced reconstruction phases on Si(111), the 5×2 has attracted the most attention and has extensively studied by experiment. [30-34]. So far, for the Ag/Si(111) system, it is widely accepted that the structure of the Ag/Si(111) $\sqrt{3} \times \sqrt{3}$ phase can be explained by the Inequivalent triangle (IET) model, which can be viewed as an asymmetrical variation of the Honeycomb Chain Trimer (HCT) model. and are supported by a number of experimental and theoretical results, while the structure of the Ag/Si(111) 3×1 phase can be explained by the honeycomb chained (HCC) model at Ag coverage of 1/3 ML. A lot of on going discussions are still on the detailed structures of Au/Si(111) (5×2) phase. Many structures are proposed including the Marks and Plass (MP) model,Hasegawa, Hosaka, and Hosoki (HHH) model based on their experimental data. Recently, two structural models, one by Riikonen and Sanchez-Portal (RS) and another by Chuang[35] were proposed independently for the Au/Si(111) (5×2)surface reconstruction.

Treating the reconstruction of semiconductor surfaces as a problem of global optimization, the recently developed genetic algorithm for structural determination of the atomic clusters and grain boundaries are presented.

In this chapter, the global structural optimizations of the Ag-induced Si(111) reconstructions were performed, which involve two types of elements in the reconstructed layers. The genetic algorithm (GA) coupled with environment-dependent Si and Ag tight-binding (TB) potentials [36] were performed for $\sqrt{3}\times\sqrt{3}$ and 3×1 phases of the Ag/Si(111) system. The low energy structural candidates selected from the GA search were further optimized using first-principles total energy calculations. Since considerable efforts have been made in the structural and electronic analysis of the Ag induced $\sqrt{3}\times\sqrt{3}$ and 3×1 phases, it is crucial to test the genetic algorithm and the TB potentials on these two phases before studying the more complex 5×2 phase. The extensive calculations showed that the previous proposed structural models, the honeycomb chain-channel (HCC) model , the inequivalent triangle (IET) models and the Honeycomb Trimer (HCT) models, are indeed the lowest energy models for the 3×1 and $\sqrt{3}\times\sqrt{3}$ phases, respectively, in both tight-binding and first-principles calculations. Moreover, a few novel structural models has been found to have lower surface energy than the double honeycomb chained (DHC) model for both Ag/Si(111) and Au/Si(111) 5×2 phases.

Another version of genetic algorithm is conducted. In the computations, we implement a variable-number genetic algorithm (GA) search in which both the number of Ag and Si atoms are variable. The structures in each generation are relaxed using DFT. The calculations are carried out within the local density approximation of DFT using projector-augmented-wave potentials,as implemented in the Vienna ab initio Simulation Package.The kinetic energy cutoff is set to 250 ev and the 4×4 Monkhorst-Pack grid is used for the surface Brillouin zone. The system is modeled as a periodically repeating slab consisting of: two fixed Si bilayers, the bottom one hydrogen passivated; a reconstructed Ag/Si layer on the top; and a vacuum gap of 0.8 nm. All the models are based on a $\sqrt{3}\times\sqrt{3}$ surface unit cell, using a Si bulk lattice constant of 0.540 nm. The two Si bilayers are fixed at the bulk crystalline positions, and the Si-H distance is fixed at 0.151 nm. The remaining Ag and Si atoms are relaxed until

the residual force is smaller than 0.25 eV/nm. The detailed results will be discussed in the following sections.

This chapter is arranged as follows: In the first section the computational methods will be discussed. GA search results are presented in the next section. Discuss and recommendation for future research are presented in the following section and conclusions will be drawn in the last section.

2 Method

The bulk truncated Si(111) surface is illustrated in Fig.2.1. The surface unit cells of $\sqrt{3}\times\sqrt{3}$, 3×1, and (5×2) phases are outlined from top to bottom in Fig.2.1. Two bulk truncated (111)-5×1 unit cells stacked along $[\bar{1}10]$ are indicated as well. The simulation cell has a slab geometry with periodic boundary conditions applied in the plane of the surface, and no periodicity in the direction normal to it. In the present work, the genetic algorithm were performed for the cases of $\sqrt{3} \times \sqrt{3}$, 3×1 and 5×1 (5×2) phases, since these phases are in STM experiment [29]. The simulation cells for tight-binding calculations contains totally four bilayers. Since naturally the intermixing between silver and silicon is limited to the top bilayer, the top bilayer atoms corresponding to a depth of $d = 3.14$ Å(measured from the position of the highest atom of a ideal bilayer) are shuffled via a set of genetic operations. In order to properly account for the surface stress, atoms in a thicker zone of second and third bilayers are allowed to relax to a local minimum of the potential energy after each genetic operation, while the bottom bilayer is kept fixed. In terms of atomic interactions, tight-binding potentials [34] are used. These potentials have superior transferability in the diverse bonding environments present on silicon surfaces [34,35]. The detailed formalism of Ag and Si tight-binding potentials is presented in the Appendix.

The development of the genetic algorithm (GA) for surface structure determination was motivated by its successful application for structural optimization of atomic clusters [18]. It has been shown that the newly developed GA is a suitable tool for high-index surface systems [15] and [16] as well as for the study of the Si magic clusters [18]. Because the optimization procedure has been described in the previous chapter, the details will not be described again here.

The difference between previous chapters and this chapter is that the mating operation involves two types of elements here. Similar to the mating operation described in the previous chapter the number of atoms n_a and n_b for each type are kept the same for every member of the pool by automatically rejecting child structures that have different numbers of atoms from their parents. The GA searches are implemented for different coverage of each type of element, corresponding to different numbers of atoms n_a and n_b in each simulation.

Since the tight-binding potentials would not give a exact energetic ordering when a large number of structures are considered, the surface energies of the models obtained from the genetic algorithm were further calculated at the level of density functional theory (DFT)[26]. The calculations in the present work were done within the generalized gradient approximation (GGA) to density functional theory using projector-augmented-wave potentials (PAW) (**?**), as implemented in VASP [27]. The kinetic energy cutoff is set to be 250 eV (18.37 Ry) and sampling (7×7), (3×9), and (2×4) of the surface Brillouin zone were used for $\sqrt{3} \times \sqrt{3}$, 3×1, and 5×2, respectively. The Si(111) surface in the DFT calculations is modeled by a periodically repeating slab of up to six layers of Si including the reconstructed surface layer and a vacuum space of 12 Å. The bottom Si bilayer was passivated by hydrogen and held fixed to simulate the bulk environment, while all other atoms above it are allowed to relax until the forces are less than 0.025 eV/Å. Theoretical bulk lattice constant of 5.465 Å was used in the surface calculations.

The surface energy γ for each surface reconstruction is calculated as follows. First, the surface energy γ_0 of a slab which is bulk truncated on both sides is calculated as follow.

$$\gamma_0 = \frac{1}{2}(E_t - N_{Si} \times E_{Si-bulk}) \tag{3.1}$$

The bulk truncated Si(111) of 6 bilayers has surface energy γ_0 =106.51 meV/Å^2. Next, surface energy difference $\triangle\gamma$ was calculated with respect to a reference slab of total energy, E_{sub}, which was bulk truncated on one side and terminated with H on the other side. $\triangle\gamma$ is expressed as

$$\triangle\gamma = (E_t - E_{sub} - \triangle N_{Si} \times E_{Si-bulk} - \triangle N_{Ag} \times E_{Ag-bulk})/A, \tag{3.2}$$

where E_t is the total energy of a considered structural model with the same substrate as in the reference slab. $\triangle N_{Si}$ ($\triangle N_{Ag}$) is the difference in number of Si (Ag) atoms relative to the reference slab and $E_{Si-bulk}$ ($E_{Ag-bulk}$) is the bulk energy of Si diamond structure (Ag fcc structure). The surface energy γ is determined as $\gamma_0 + \triangle\gamma$. The reference slab for our DFT calculations is a hydrogen-passviated two-bilayer substrate. The total energies of the structural models are calculated using the hydrogen-passviated three-bilayer substrate including the reconstructed layer.

3 Results and discussions

Ag/Si(111) $\sqrt{3} \times \sqrt{3}$ phase

Since 8 structural models of $\sqrt{3} \times \sqrt{3}$ phase were included in the fitting of the Ag-Si TB potentials (also see Appendix), the structural optimizations of the $\sqrt{3} \times \sqrt{3}$ phase were performed first. Selected structural models obtained from GA search at various Ag and Si coverages are further optimized using first-principles calculations. The surface energies of selected models are plotted in Fig.2.3 The results show that Si-Ag tight-binding potentials can basically reproduce the results of DFT calculations except for a few structure where Ag atoms are found underneath the Si surface layer and hence have higher coordination than the Ag atoms on the surface.

Most importantly, the lowest energy model using TB calculations remains the lowest using DFT calculations. The GA search retrieved the same lowest energy structures. The lowest energy structure corresponds to Ag coverage of 1 ML Ag and Si coverage of 1 ML. The lowest energy structural model of such a coverage is identified as the honeycomb trimer (HCT) model.

Since the HCT model has also been well-studied elsewhere[28], further electronic analysis will not be performed here.

In the genetic algorithm coupled with DFT potential search, we implement a variable-number genetic algorithm (GA) search in which both the number of Ag and Si atoms are variable. The structures in each generation are relaxed using DFT. The calculations are carried out within the local density approximation of DFT using projector-augmented-wave potentials, as implemented in the Vienna ab initio Simulation Package.The kinetic energy cutoff is set to 250 eV and the 4x4 Monkhorst-Pack grid is used for the surface Brillouin zone. The system is modeled as a periodically repeating slab consisting of: two fixed Si bilayers, the bottom one hydrogen passivated; a reconstructed Ag/Si layer on the top; and a vacuum gap of 0.8 nm. All the models are based on a $\sqrt{3} \times \sqrt{3}$ surface unit cell, using a Si bulk lattice constant of 0.540 nm. The two Si bilayers are fixed at the bulk crystalline positions, and the Si-H distance is fixed at 0.151 nm. The remaining Ag and Si atoms are relaxed until the residual force is smaller than 0.25 eV/nm.

Figure 8 shows results of the GA search for different types of $\sqrt{3} \times \sqrt{3}$ structures. In order to show the variation in both Si and Ag coverage, we introduce a 2-digit notation for the x-axis, the 1st digit being the number of Si atoms and the 2nd being the number of Ag atoms. In the bottom x-axis labels, these numbers are normalized to the (1x1) unit cell area, and in the top axis these numbers are normalized to the $\sqrt{3} \times \sqrt{3}$ unit cell area. The point with the lowest Ef has x = (1,1) per (1×1). This is the IET structure. The energy of the (7×7) is shown by the blue line.

Ag/Si(111) 3×1 phase

Since the 3×1 phase has also been well-studied, structural optimizations of the 3×1 phase were performed at Ag coverage of 1/3 ML and at various Si coverages. The Ag coverage of 1/3 ML is chosen according to the well-accepted honeycomb chain-channel (HCC) model[23]. Selected structural models at each Si coverage are further optimized using first-principles calculations. The surface energies of selected structural models versus Si coverage are plotted in Fig. 3.3. The plot shows that the surface energies calculated using tight-binding potential are in good agreement with those calculated using first-principle method except for two structures at Si coverage of 1 ML which Ag atoms are found underneath the Si surface layer. In order to clarify the plot in Fig.3.4(a), only the lowest surface energies versus Si coverage are plotted in Fig. **??**(b). The plot shows that the lowest energy model corresponds to Ag coverage of 1/3 ML and Si coverage of 4/3 ML. The structural model at this coverage is identified as the honeycomb chained (HCC) model, as well as several low energy models at this coverage are illustrated in Fig. 3.4. Fig.3.4.(a), (b), (c), and (d) are models with the honeycomb chained (HCC) feature with Ag atoms at different positions. Fig.3.5(e) is another model obtained from our GA search. Since the HCC model for the 3×1 phase has been well studied, further electronic analysis of HCC model will not performed here.

Similar to the $\sqrt{3} \times \sqrt{3}$ case, we also showed GA search results for the 3×1 phase here with the other method. The lowest energy structure is the HCC structure, with 2 Ag atoms and 3 Si atoms on the surface unit cell, as shown in Fig 3.4.

Ag/Si(111) 5×2 phase

As the surface area of the reconstruction increases, the number of the combinations of Ag and Si coverage increases in the order of $O(N^2)$. For the 5×2 phase of Ag/Si(111) system, there is no model proposed after the first report of the phase diagram [2]. However, the Au/Si(111) surface also exhibits 5×2 and 5×1 phases. The Au coverage has been determined precisely to be 2/5 ML experimentally. There are numerous studies of Au/Si(111) 5×2 and 5×1 phases at this Au coverage. Among them, the double honeycomb chained (DHC) model is the lowest energy model for 5×1 and 5×2 in the literature [26]. DHC model of the 5×2 phase can be obtained by removing one atoms every two 5×1 cells. Structural optimizations of 5×1 phase at Ag coverage of 2/5 ML were performed at various Si coverages. Selected structural models are further optimized using first-principles calculations. The lowest surface energies versus Si coverage as well as the DHC model are plotted in Fig.3.4.2 at Ag coverage of 2/5 ML. The plot shows that the lowest energy group is at Si coverage of 7/5 ML. The structure model obtained at this coverage is found to have lower surface energy than DHC model by 5 meV/Å^2. The selected low energy models from our search and the DHC model are shown in Fig. 3.5

Knowing that the DHC model of 5×2 phase removes the bridged Si atom from bridged DHC model every two 5×1 cells, several structural models of 5×2 phase were created from other 5×1 search and optimized using first-principles calculations. One model of 5×2 phase is found to have lower surface energy than the DHC model by 5 meV/Å^2. The structural models of 5×2 phase as well as the DHC model 5×2 are shown in Fig. **??**. The simulated STM image of new model and DHC model are calculated and shown in Fig. 3.6(a) and (b) at the sample bias of -1.0V.

Au/Si(111) 5×2 phase

We first systematically examine the atomic and electronic structures of the honeycomb chain models for Au/Si(111) (5×2) surface by using first principles calculations.

Despite the numerous models that have been proposed previously, differences in surface energies among these models are found to be rather small.Furthermore, all of these models exhibit a HC (HoneyComb) feature. Thus, a question arises as to what kind of optimal atomic arrangement the lowest energy model should have. It is therefore highly desirable to perform a comprehensive study on the honeycomb chain feature. we systematically examine the atomic and electronic structures of the honeycomb chain models for Au/Si(111) 5×2 surface by using first principles calculations. First, the gold chains are combinatorially assigned on the honeycomb chain structure in order to generate a series of HC models. Overall, 36 models are generated using this method and further optimized. Among these 36 models, we are able to identify four previously proposed models, (Marks and Plass, Erwin, Chuang, and Riikonen and Sanchez-Portal). In addition, we have identified a new model, which is lowest in surface energy.

The atomic structure of the HC model is illustrated in Fig. The numbers in the figure are used to label the positions of two gold chains along the (1- 10) direction. The 5×2 unit cell is outlined with red dotted lines. Gold, surface silicon, and the underlying silicon atoms are illustrated in blue, yellow, and white, respectively. To explore all the honeycomb chain models, the gold chains are first combinatorially assigned on the honeycomb chain structure to generate a series of 5×1 HC models. This method yielded 36 models, which are subject to further optimizations. The relative surface energies of selected important models are plotted in Fig.. The lowest energy honeycomb chain model turns out to be HC16, whose atomic structure is illustrated in Fig.. We are also able to identify four earlier proposed models, namely, HC35, HC18, HC15, and HC13 which stand for Marks and Plass, Erwin, Chuang,and Riikonen and Sachez-Portal,respectively. However, they all have higher surface energy than the HC16(5x1) model. A prior study indicated that the MP model (HC35) and Erwin model (HC18) are of different orientations with respect to the underlying substrate. Our own model nomenclature also allows us to label models, which have the same motif but different orientations with respect

to the substrate. Our calculations show that the substitution of Si atoms with Au atoms for all the models basically preserves the honeycomb structure. The relative surface energies as well as the separations between the left (L) and the right (R) gold rows in the (5×1) phase are summarized in Fig 3.8. We note that the separation of the two gold rows in the HC16 model is the largest $7.47A$ while that in the RS is the smallest $3.10A$.

Having identified the (5×1) model, the (5×2) models can be created using the following schemes. First, following Marks and Plass's procedure, the (5×2) phase is created by adding one Si atom on every other (5×1) cell,18 noting that for each of the (5×1) models there are four honeycomb sites on which to place the Si adatoms. Second, using Erwin's prescription, we remove a Si atom in every other (5×1) cell in order to create a (5×2) model.Since there are seven Si atoms in each (5×1) cell, seven models for (5×2) can be created using the latter technique of removing Si atoms. Third, instead of atom removal, the (5×2) model is artificially produced via the creation of an asymmetric bulge of silicon atoms in the row as was employed by Riikonen and Sanchez-Portal.Based on this idea, it is possible to create a new (5×2) model by displacing or distorting some atoms in two (5×1) cells. Last, one can combine these three methods to create the (5×2) cell as was done in our previous study.23 In short, we have applied the above approaches to the newly identified HC16 (5×1) model and have generated up to 40 (5×2) models out of it. Of these, we are able to identify one (5×2) model that is the lowest energy model and which has not been previously reported.

We found that though the removal of Si atom effectively preserves the honeycomb structure, a rebonded motif of a trimer and a pentamer ring with neighboring atoms is observed in some cases. This pattern has also been seen in a previous study. We also found that the removal of a silicon atom in the Erwin model lowers the surface energy by 94 meV per (5×2) cell in agreement with the previous work by Erwin. In some cases, removing every other Si atoms in a row increases the surface energies. Likewise, adsorption of an adatom could also result in lower or higher surface energy depending on the location of the adsorption site.

The surface energies of the HC16 (5×1) and HC16 (5×2) models are found to be lower than that of Erwins. More significantly, the present results indicate that among the models

considered here the HC16 (5×2) variant is the most stable in energy. The rearrangement of one gold row in the HC16 (5×2) leads to a 178 meV per (5×2) cell lowering of total energy with respect to the HC16 (5×1) case.

In summary, models with the honeycomb chain feature for the Au/ Si(111)-(5×2) surface reconstruction were systematically examined using first-principles calculations. Our calculations showed that the HC16(5×2) model is energetically more stable than any proposed models in the literature. More importantly, the strong surface band observed in angle resolved photoemission was well reproduced in the HC16(5×2) model. Additionally, the simulated STM image of this model also recovered the Y-shaped feature seen in the experimental STM images.

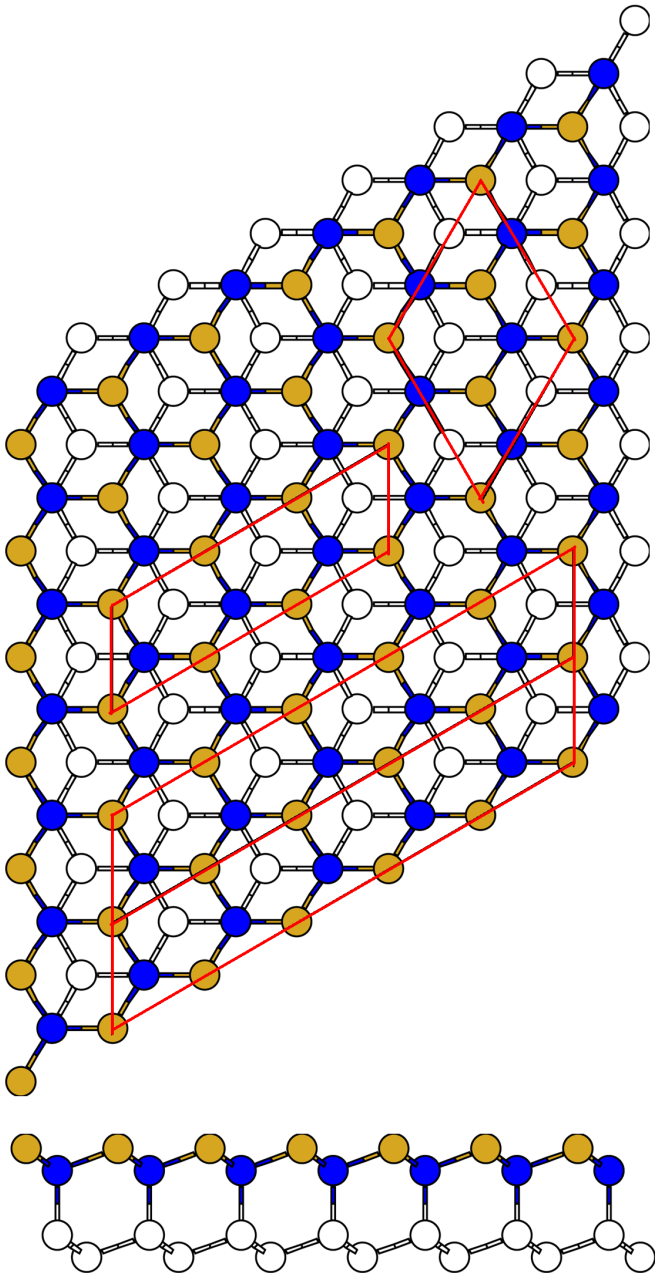

Figure 3.1 Top and side views of a unreconstructed Si(111) 7×7 surface. The unit cells of $\sqrt{3} \times \sqrt{3}$, 3×1, and 5×2 are outlined at top, middle and bottom, respectively. The Si atoms in top two layers are colored gold and blue, respectively; the Si atoms in the second bilayer is colored white.

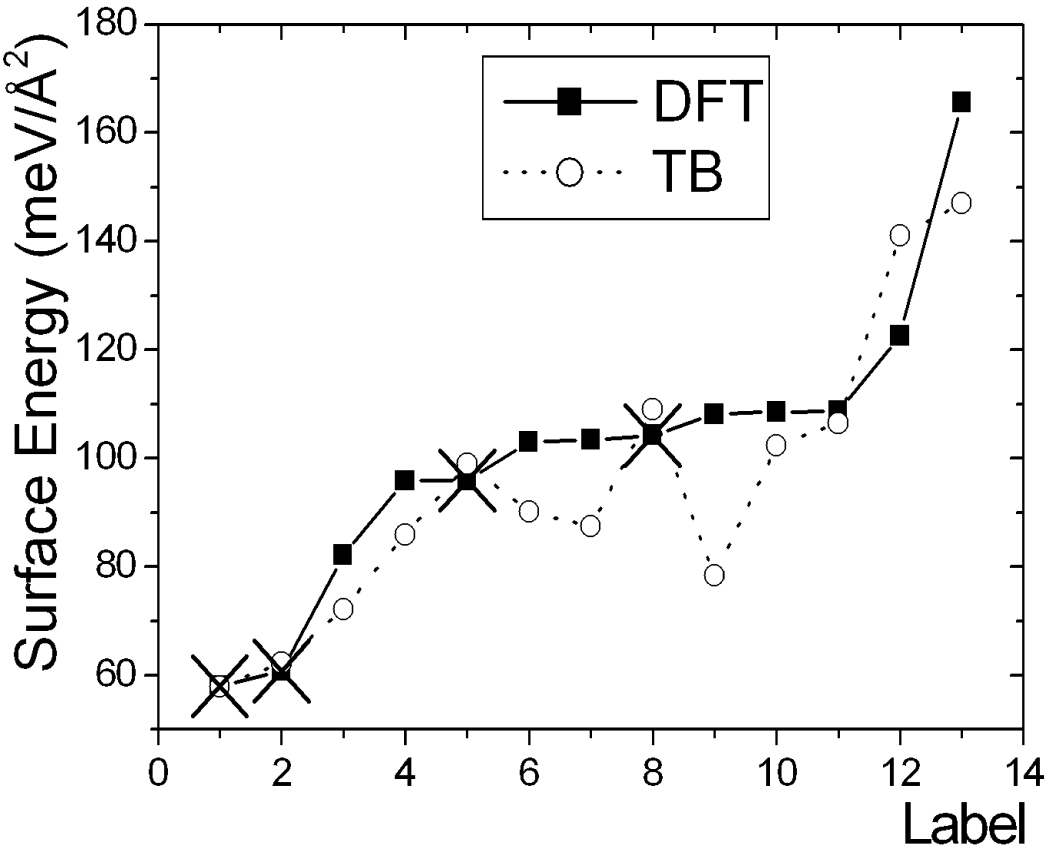

Figure 3.2 Surface energies of selected models using first-principles and tight-binding calculations for the $\sqrt{3} \times \sqrt{3}$ phase. The big Xs are the models involving Ag-Si TB potential fitting.

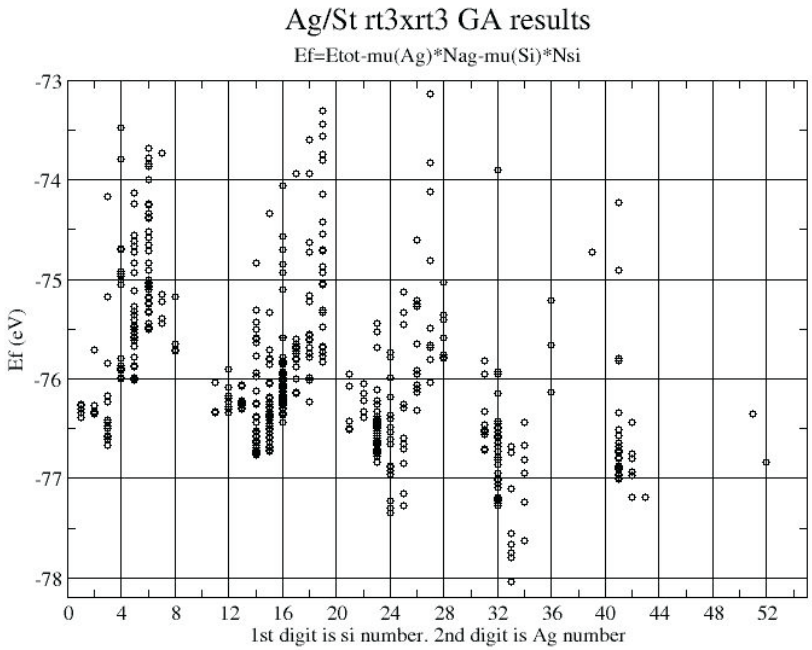

Figure 3.3 GA search for different types of $\sqrt{3} \times \sqrt{3}$ structures.

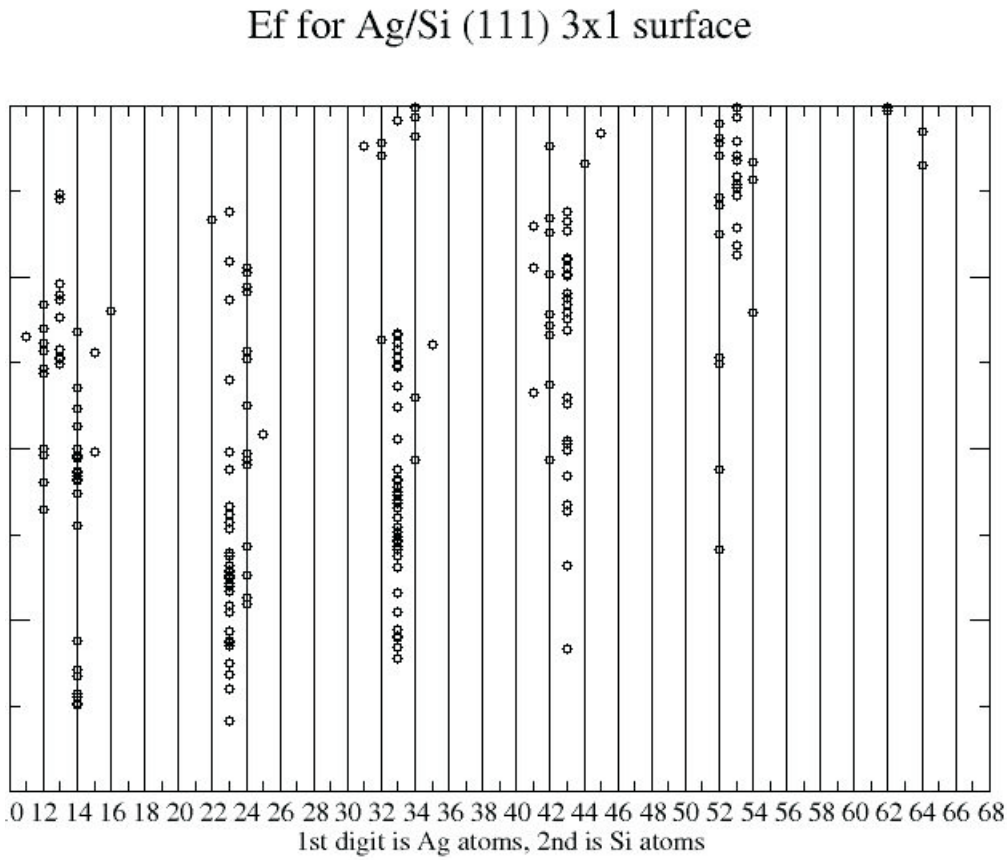

Figure 3.4 GA search for different types of 3×1 structures.

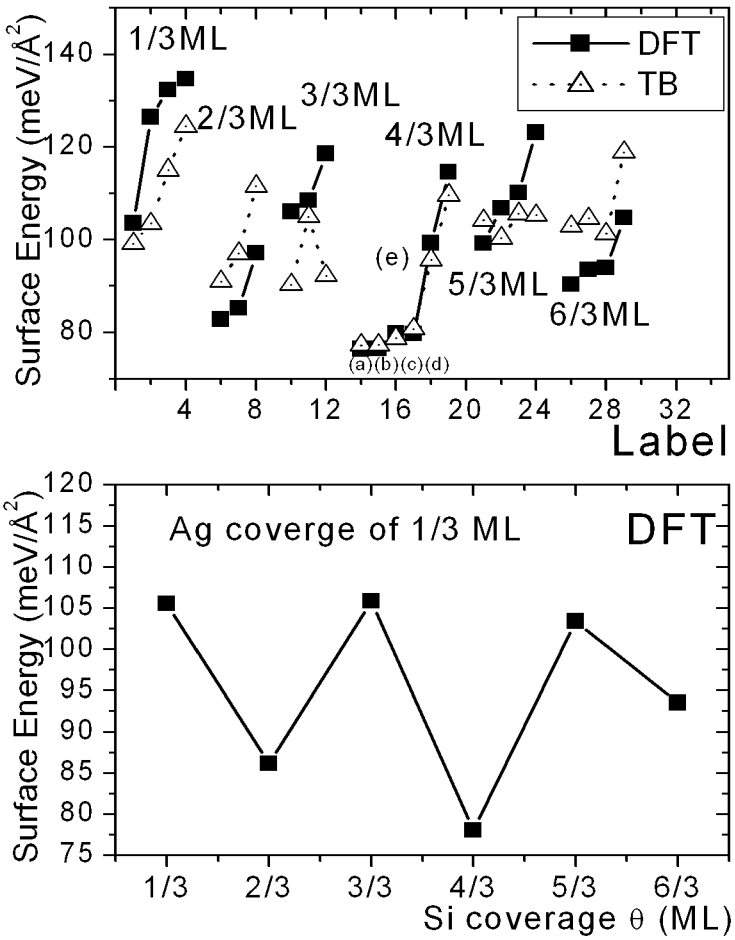

Figure 3.5 Top: Surface energies of selected models using first-principles and tight-binding calculations versus Si coverage for the 3×1 phase at Ag coverage of 1/3 ML. Bottom: The lowest surface energies using first-principles calculations versus Si coverage for the 3×1 phase at Ag coverage of 1/3 ML. The plot shows that the reconstruction with lowest surface energy is at Si coverage of 4/3 ML.

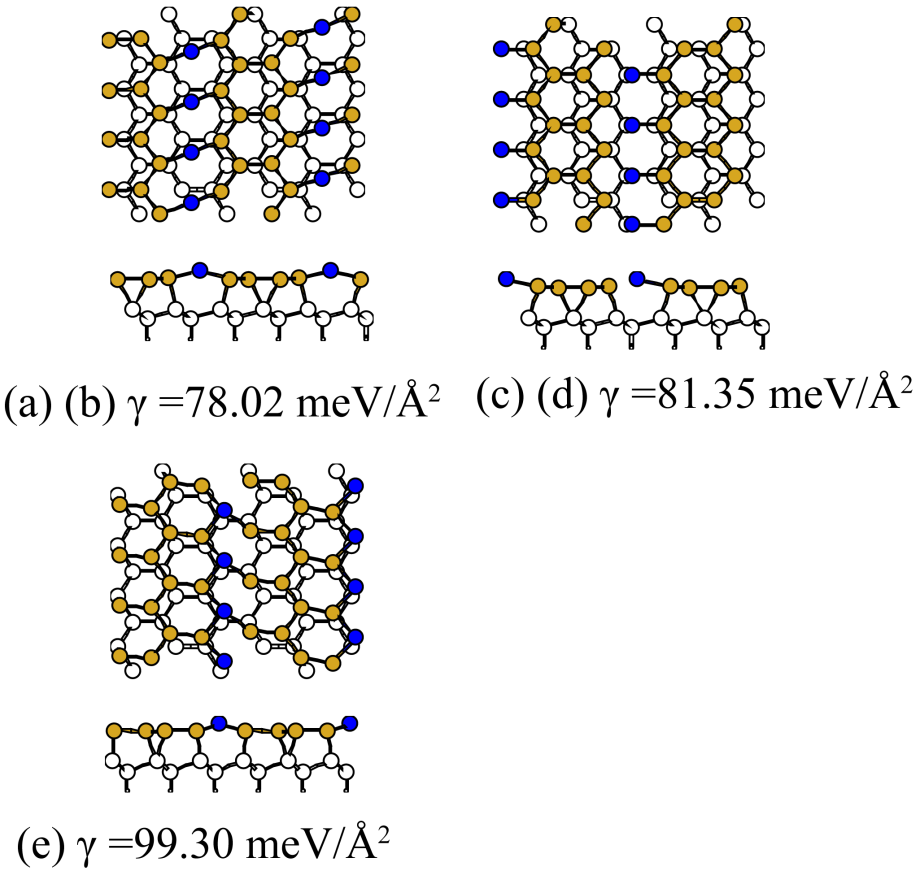

Figure 3.6 The low energy structural models of Ag/Si(111) 3×1 phase at Ag coverage of 1/3 ML and Si coverage of 4/3 ML. (a) and (b) are models of mirror symmetry, while (c) and (d) are models of mirror symmetry. They are all honeycomb chained (HCC) models with the Ag atoms at different positions. (e) is another models of this coverage. The Ag atoms are colored blue. The Si atoms in the reconstructed layer are colored gold, while the Si atoms in the substrate are colored white. The surface energies in the figure are done using DFT calculations with the two-bilayer substrate. Only one bilayer is shown in the figure.

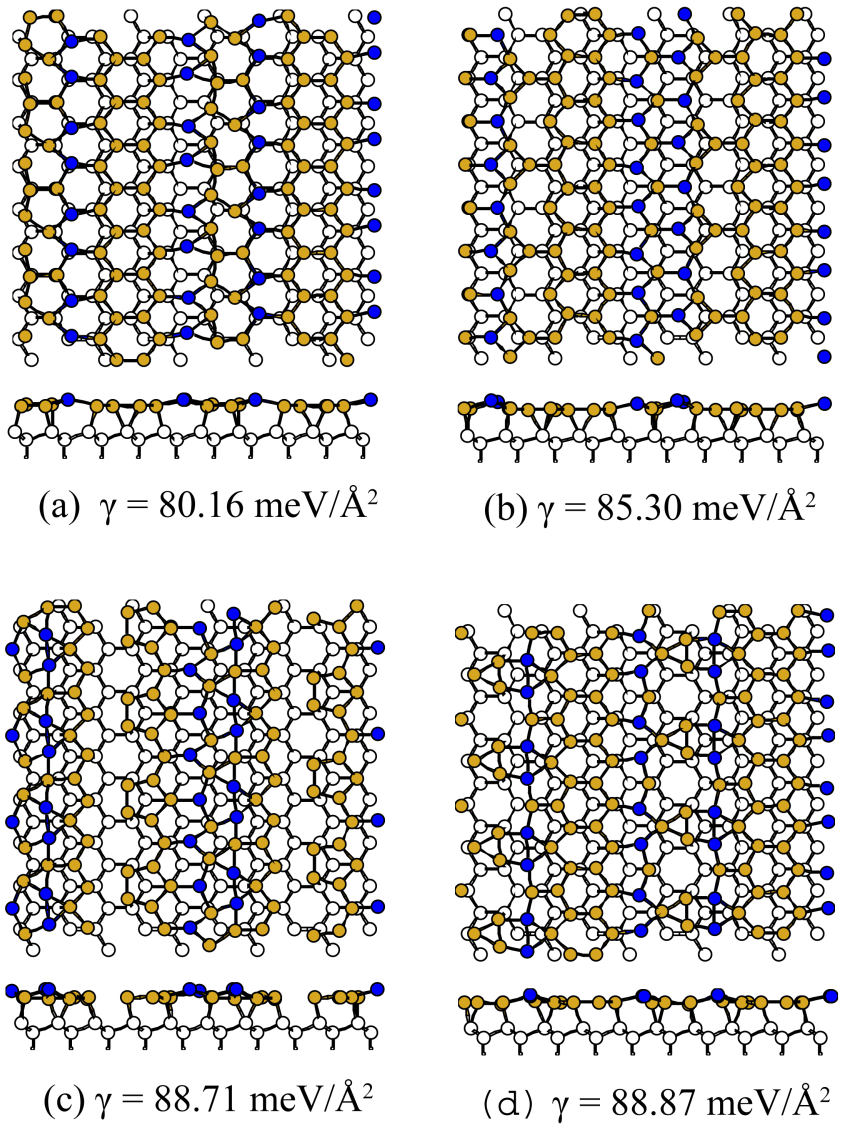

Figure 3.7 The low energy structural models for Ag/Si(111) 5×2 phase at Ag coverage of 2/5 ML and and Si coverage of 6.5/5 ML. (a) is obtained from GA search. (b) is the DHC model. (c) and (d) are other low energy models from GA search. The Ag atoms are colored blue. The Si atoms in the reconstructed layer are colored gold, while the Si atoms in the substrate are colored white. The surface energies in the figure are done using DFT calculations with the two-bilayer substrate. Only one bilayer is shown in the figure.

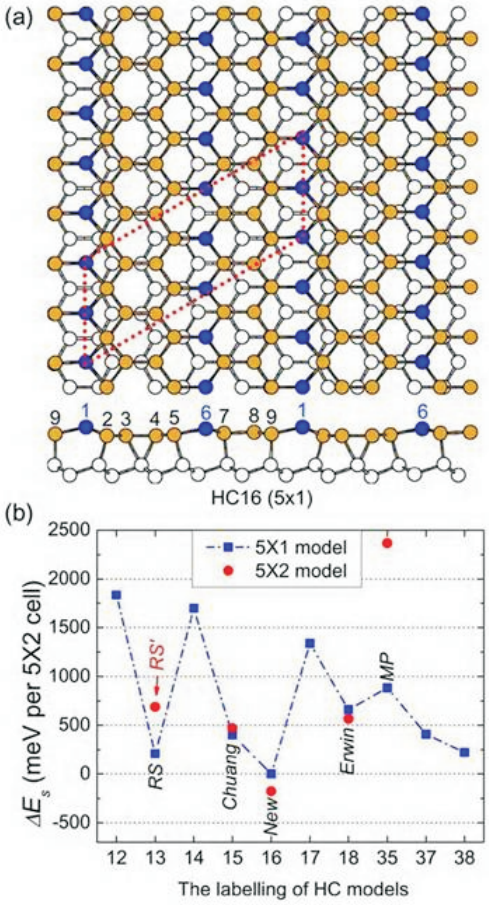

Figure 3.8 (a)Atomic structure of the double honeycomb chain model. The numbers in the figures are used to label the positions of gold chains along the (1-10) direction. The 5×2 unit cell is outlined in red. (b) The relative surface energy with respect to the HC16 model

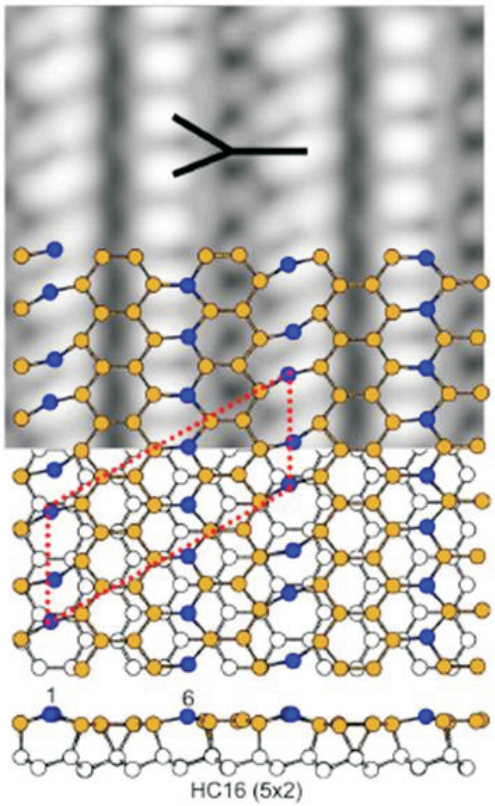

Figure 3.9 Simulated filled-state STM image with a sample bias of 0.8 eV and atomic structure of the HC16 (5×2) mode

CHAPTER 4. A simple model for the thermal radiation spectrum of a system with non-uniform temperature

1 Introduction

Using a simple model, we show that the thermal radiation from a system with non-uniform temperature can exceed the intensity of an isothermal blackbody with the same average temperature. The results suggest that recent observations of exceedingly high thermal emission from tungsten photonic crystals are not necessarily in conflict with fundamental laws of thermodynamics.

Recent experimental observation of thermal radiation from metallic photonic crystal systems revealed a surprising result: the samples emitted more radiation than a blackbody of the same temperature in certain spectral regions[62-64]. This observation has created a lot of controversy because it seems to contradict the second law of thermodynamics. In this paper, we utilize a simple model to look at this phenomenon in more detail and show that under the experimental conditions, it might be possible to obtain a description of the observed facts without violating any fundamental laws of thermodynamics.

2 Experiment

The experiments were performed on 3D tungsten photonic–crystal fabricated with a modified silicon process[62, 63]. In the experiment the fabricated 3D tungsten crystal was biased by applying a voltage across the sample and heated through Joule heating[63]. The experimental observation indicated that in a certain wavelength range the emission power of the sample was larger than that of a blackbody with the same temperature[63]. The key to the resolution of

this apparent conflict with Kirchkoff's law lies in the fact that the experimental system is in a steady state but not at thermal equilibrium. Thus, the system is actually not described by a single uniform temperature but by a varying temperature distribution over the various parts of the system. In the previous papers, the thermal radiation from the system is compared with a blackbody with the same averaged temperature. We will show in this paper that under these conditions, the thermal radiation from the system cannot be characterized by a single temperature and that, in the high frequency region, it is indeed possible to obtain enhanced radiation much above that from a blackbody with the same average temperature.

3 Model details

In the experiments, the effective temperature, averaged over the entire sample, is determined by measuring sample resistivity and comparing it to the calibrated temperature– dependent tungsten resistivity[56]. However, details of the temperature distribution of the photonic crystal filament were not available and it is quite possible that there are 'hot spots' in the experimental system. Lacking detailed information on the temperature distribution of the experimental sample, we adopted a simple model assuming the sample can be divided into two regions with fractions $1-\alpha$ and α, each with temperature $T1$(500K) and $T2$(3000K) respectively. In one calculation, $T2$ is chosen to be near the melting temperature of tungsten. We also repeat our calculations assuming different ratios of T2 and T2 later. From the resistivity of the whole sample, the effective temperature $< T >$

$$< T >= (1-\alpha)T1 + \alpha T2 \tag{4.1}$$

$< T >$ and α are shown in Fig. 4.1

In standard treatments of blackbody radiation, the energy flux is given by

$$dj_{bb}(\lambda) = \frac{2hc^2}{\lambda^5}\frac{1}{exp(\frac{hc}{\lambda kT})-1}d\lambda d\Omega \tag{4.2}$$

In our model, the total flux can be obtained by adding the contributions from the two parts of the system with different temperatures. substitute$\frac{1}{exp(\frac{hc}{\lambda kT})-1}$ with $\frac{1-\alpha}{exp(\frac{hc}{\lambda kT1})-1} + \frac{\alpha}{exp(\frac{hc}{\lambda kT2})-1}$ to

get the energy flux in the model

$$dj(\lambda) = \frac{2hc^2}{\lambda^5}(\frac{1-\alpha}{exp(\frac{hc}{\lambda kT1})-1} + \frac{\alpha}{exp(\frac{hc}{\lambda kT2})-1})d\lambda d\Omega \tag{4.3}$$

Given the effective temperature of the sample$< T >$, α can be decided by the relation $< T >= (1-\alpha)T1 + \alpha T2$

Since the sample is not an ideal blackbody. The absorptance of the sample should be considered. A Gaussian function, shown in Fig. 4.2, is used to simulate the absorptance curve, shown in Fig. 4.3.

In the model the radiation of the sample becomes

$$dj(\lambda) = \frac{2hc^2}{\lambda^5}(\frac{1-\alpha}{exp(\frac{hc}{\lambda kT1})-1} + \frac{\alpha}{exp(\frac{hc}{\lambda kT2})-1})G(\lambda)d\lambda d\Omega \tag{4.4}$$

$G(\lambda)$ is the function of absorptance of the sample.

Let the effective temperature $< T >$ be $1190K$,$1320K$,$1440K$,$1535K$ respectively. We can make a comparison between the two graphs from the experimental data in Fig. 4.4 and the model used in Fig. 4.5.

From the comparison the result of the model confirms that in a certain region of wavelength(about $0-3\mu m$), the radiation power exceeds the blackbody of the same effective temperature. It is not the violation of the second law of thermodynamics, because of the fact that our sample is not uniform in temperature. While it is true that an object with a uniform temperature can never emit more power than a blackbody with the same temperature, our model shows that the sample, having two parts with different temperatures, is able to emit more power than a blackbody with the same effective temperature. Also the wavelength corresponding to the peak region in the model at $\lambda \approx 1.8\mu m$, shown in Fig. 4.5 is very close to the experimental observation in Fig. 4.4.

In the model above, T1 and T2 have specific values. We can vary the values of T1 and T2 by changing the ratio of $\frac{T2}{T1}$ and still get similar results as in the model. Neglecting absorptance, consider

$$f = \frac{dj(\lambda)}{dj_{bb}(\lambda)} = \frac{\frac{1-\alpha}{exp(\frac{hc}{\lambda kT1})-1} + \frac{\alpha}{exp(\frac{hc}{\lambda kT2})-1}}{\frac{1}{exp(\frac{hc}{\lambda k<T>})-1}} \tag{4.5}$$

$$< T >= (1-\alpha)T1 + \alpha T2 \tag{4.6}$$

choose $\lambda = 1.8\mu m$, since $exp(\frac{hc}{\lambda kT}) \gg 1$

$$f \doteq \frac{\frac{1-\alpha}{exp(\frac{hc}{\lambda kT1})} + \frac{\alpha}{exp(\frac{hc}{\lambda kT2})}}{\frac{1}{exp(\frac{hc}{\lambda k < T >})}} = (1-\alpha)exp(\alpha\frac{hc}{\lambda k < T >}(1-\frac{T2}{T1})) + \alpha exp((1-\alpha)\frac{hc}{\lambda k < T >}(1-\frac{T1}{T2})) \tag{4.7}$$

Take $\frac{T2}{T1} = 4$ and $\frac{T2}{T1} = 2$ respectively. From Fig. 4.6 and Fig. 5.5, we have $f = \frac{dj(1.8\mu m)}{dj_{bb}(1.8\mu m)} > 1$, which verifies that the radiation power intensity from a system with non-uniform temperature can exceed the intensity of an isothermal blackbody with the same effective temperature.

In the simple model here only two different temperatures are assumed. In the real sample, however, there may exist a temperature distribution. The effective temperature can still be used for averaging over the entire sample. Suppose there exist a set of different temperatures T_1, T_2,..., T_n, which have fractions α_1, α_2,..., α_n respectively. The total effective temperature will be

$$< T >= T_1\alpha_1 + T_2\alpha_2 + ... + T_n\alpha_n \tag{4.8}$$

with

$$\sum_{i=1}^{n} \alpha_n = 1 \tag{4.9}$$

when neglecting absorptance, the total radiation of the sample

$$dj(\lambda) = \sum_{i=1}^{n} dj_i(\lambda) = \frac{2hc^2}{\lambda^5}(\sum_{i=1}^{n} \frac{\alpha_i}{exp(\frac{hc}{\lambda kT_i}) - 1})d\lambda d\Omega \tag{4.10}$$

consider the two parts α_1 and α_2, the effective temperature over the two parts is $< T >_{12}$.

$$< T >_{12} = \frac{\alpha_1 T_1 + \alpha_2 T_2}{\alpha_1 + \alpha_2} \tag{4.11}$$

similar to the calculations in the model, we will have

$$f_{12} = \frac{dj_1(\lambda) + dj_2(\lambda)}{dj_{12}(\lambda)} > 1 \tag{4.12}$$

$dj_{12}(\lambda)$ is the radiation power of parts α_1 and α_2 together with a uniform temperature $< T >_{12}$. So further with part α_3 we will have

$$dj_1(\lambda) + dj_2(\lambda) + dj_3(\lambda) > dj_{12}(\lambda) + dj_3(\lambda) > dj_{123}(\lambda) \tag{4.13}$$

By repeating we get

$$\sum_{i=1}^{n} dj_i(\lambda) > dj_{12\ldots n}(\lambda) = dj_{bb}(\lambda) \tag{4.14}$$

with n becomes infinity T_i and α_i will be continuous and $\sum$ will become $\int$.

4 Conclusions

By using a simple model, we explained that recent observations of exceedingly high thermal emission from tungsten photonic crystals are not necessarily in conflict with fundamental laws of thermodynamics. Results from the model were compared with the experimental data and further discussions were made.

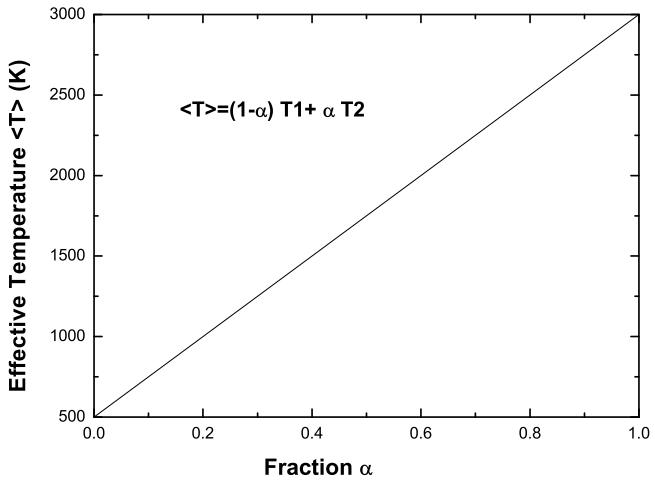

Figure 4.1 The temperature over the sample is not uniform. In the model we assume the sample has two parts with different temperatures $T1$ and $T2$. The effective temperature, average over the entire sample, can be demonstrated by $T1$, $T2$ and α in this model. Different fraction α will result in different effective temperature.

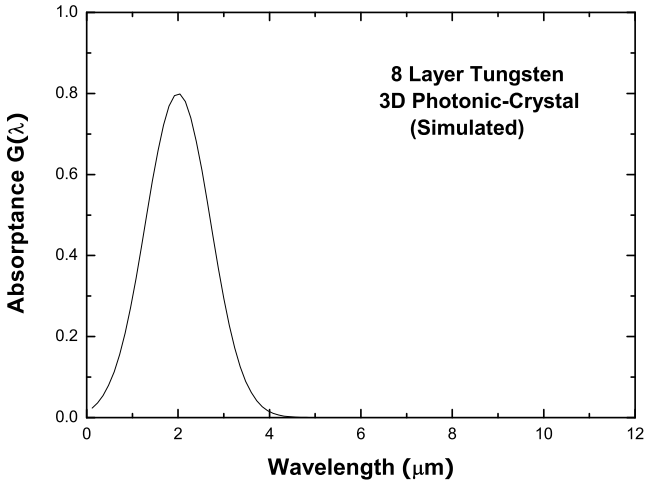

Figure 4.2 Simulated absorptance of the sample using a Gaussian function. the simulated function is easier to use for calculation of the radiation of the sample with enough accuracy needed.

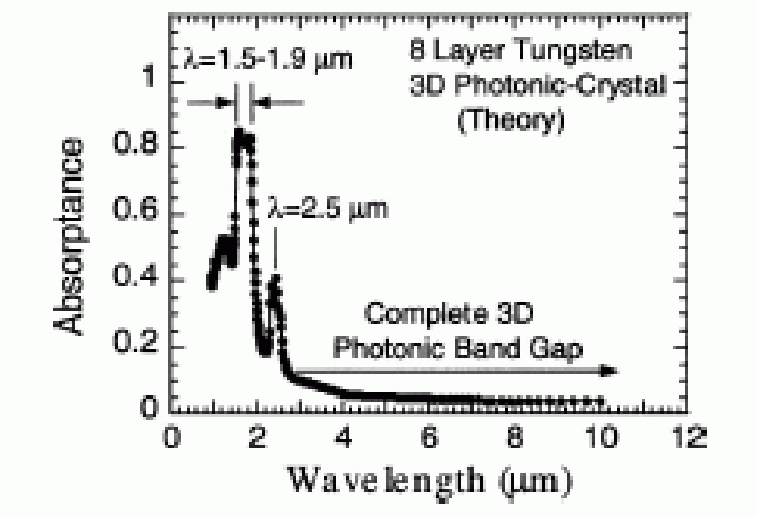

Figure 4.3 It is the computed absorption spectra for an eight–layer 3D tungsten photonic–crystal sample. In the model a Gaussian function is used to simulate the curve in the graph.

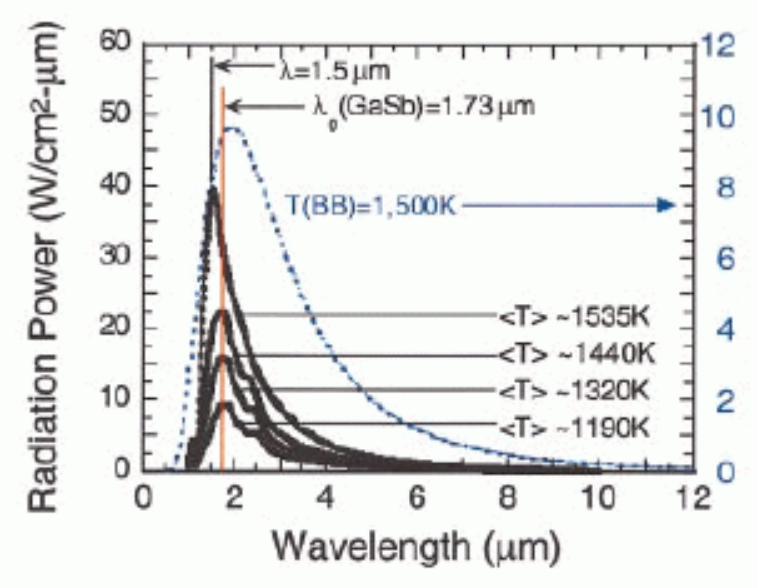

Figure 4.4 From the experiment it shows the measured photonic–crystal emission power at the effective temperature 1190, 1320, 1440 and 1535K, respectively. The dashed line is a blackbody radiation curve. From the graph the radiation power of the sample exceeds that of a blackbody in certain spectral regions.

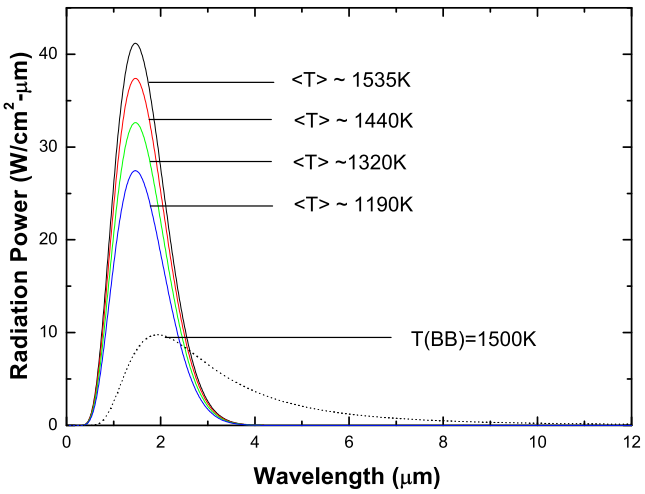

Figure 4.5 Results of the radiation power using the simple model, consisting different effective temperatures corresponding to the experimental data. The dashed line is a blackbody radiation.

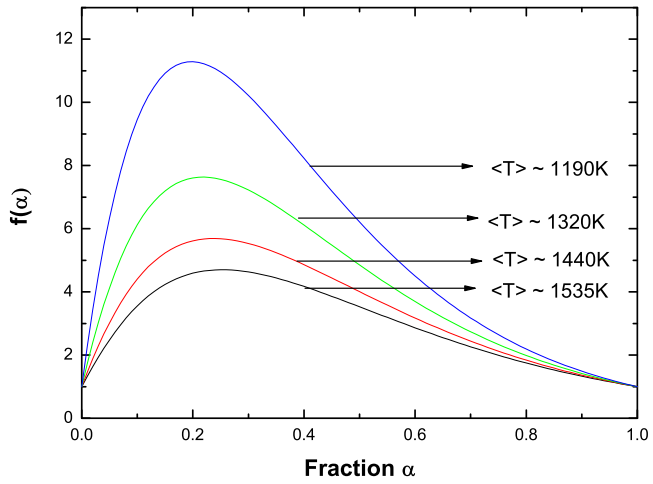

Figure 4.6 At wavelength $\lambda = 1.8\mu m$, $\frac{T2}{T1} = 4$, $f(\alpha)$ versus α for different effective temperature $< T >$

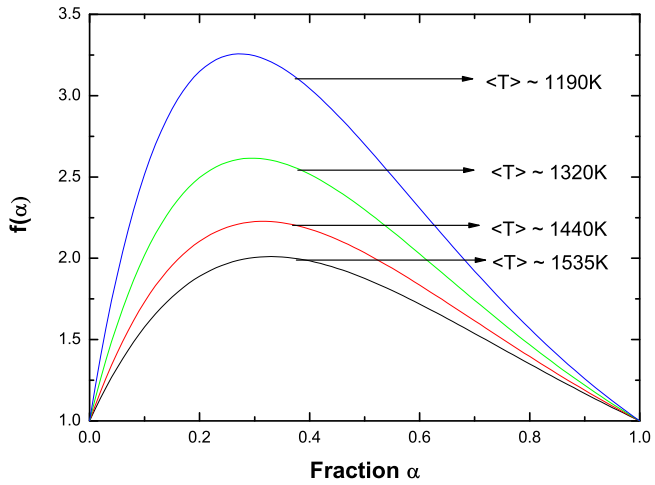

Figure 4.7 At wavelength $\lambda = 1.8\mu m$, $\frac{T2}{T1} = 2$, $f(\alpha)$ versus α for different effective temperature $< T >$

CHAPTER 5. Exceedingly high thermal radiation from 3D metallic photonic crystals: A simple model

1 Introduction

Recent experimental observation of thermal radiation from metallic photonic crystal structures revealed a surprising result: the samples emitted more radiation than a blackbody of the same temperature in certain spectral regions. Using a simple model, we show that the temperature distribution can be strongly inhomogeneous across the tungsten lattice sample under Joule heating. As a result, thermal radiation from the metal sample can exceed the intensity of an isothermal blackbody with the same average temperature. The results suggest that the observations of exceedingly high thermal emission from the tungsten photonic crystals are not necessarily in conflict with fundamental laws of thermodynamics.

In the past decade photonic crystals made from dielectric or metallic building blocks have attracted a vast amount of interest due to their power to control the propagation of light at the subwavelength scale [68-73]. Besides applications in conventional areas such as filters, polarizers, beam splitters, and mirrors in the microwave and infrared regimes [75-80], metallic photonic crystals have found a new frontier of application as high-efficiency thermal radiation source for incandescent lamp and thermal photovoltaic power generation [81-94]. This power has been brought about by the existence of photonic band gaps and the accompanying modification of the photon density of states [85-88].

Recent experimental observation of thermal radiation from three-dimensional (3D) tungsten photonic crystal structures revealed a surprising result: The samples emitted more radiation than a blackbody of the same temperature in certain spectral regions [82-84]. This observation has created a lot of controversy because it seems to contradict the second law of thermodynamics

[88-100]. In this paper, we utilize a simple model to look at this phenomenon and show that under the experimental conditions, it might be possible to obtain a description of the observed facts without violating any fundamental laws of thermodynamics.

The geometric structure of a 3D tungsten photonic crystal is shown in Fig. 5.1(a). The metallic sample is biased by applying a voltage and heated through Joule heating [81-83], as schematically depicted in Fig. 5.1(b). The hot sample then becomes a thermal radiation source. A typical measurement result of the thermal emission spectra is displayed in Fig. 2 at different bias voltages V as 3, 4, 5, and 6.5 V. The corresponding measured total electric current flowing through the sample is 1.69, 2.04, 2.32, and 2.84 A. The total resistance R is obtained by $R = V/I$ and is found to be 1.78, 1.96, 2.16, and 2.29 Ohm. The ratio of this resistance to the room temperature resistance of the sample is compared to the calibrated temperature-dependent tungsten resistivity (measured from a homogeneous thin film) to determine the average temperature of the sample. The results are 1190, 1320, 1440, and 1535 K at the four values of bias voltages. In Fig. 5.2, the thermal emission spectrum from a 1500K blackbody is also shown as a reference. In a certain wavelength range (1-3 μm) the peak emission power of the 1535K tungsten sample is more than 3 times larger than that of the 1500K blackbody. This result seems to be in conflict with Kirchhoff's law and the second law of thermodynamics.

The key to the resolution of this apparent conflict lies in the fact that the experimental system is in a steady state but not at thermal equilibrium. Thus, the system is actually not described by a single uniform temperature but by a varying temperature distribution over the various parts of the system. As the temperature of the sample is determined by measuring the resistivity of the whole sample, the temperature determined is the average temperature of the tungsten sample. We will show that a non-uniform temperature distribution can indeed lead to enhanced radiation much above that from a blackbody with the same average temperature. A simplified model is adopted to determine such a temperature distribution and the corresponding thermal radiation power from the tungsten photonic crystal sample.

In the experiment, the tungsten photonic crystal samples are 10mm(L) long, 2mm(w) wide, and 6μm (h) thick. In principle, the temperature distribution due to Joule heating in this

inhomogeneous network is quite complicated. However, we note that the sample is very thin and the width is also much smaller than the length. Therefore, the main temperature variation is along the length of the sample and we can adopt a one-dimensional model to approximate the sample as an effective homogeneous metal plate with length L and an effective cross area $S_{eff} = fwh$. Here f is the effective filling fraction of the network sample. The schematic of the model system is depicted in Fig. 3. In this model, I is the current flowing through the sample in the x direction. $T(x)$ is the temperature of the sample as a function of x.

In the steady state, let us consider a small segment with length Δx. From energy conservation $P_I = P_{conduction} + P_{radiation}$ we find the following relation:

$$I^2 R = -K(T) S_{eff} \frac{d^2T}{dx^2} \Delta x + \sigma e(T)(T^4 - T_0^4)(2w\Delta x), \tag{1}$$

which yields

$$I^2 \frac{\rho(T)}{fwh} = -K(T) \frac{d^2T}{dx^2} fwh + 2\sigma e(T)(T^4 - T_0^4)w. \tag{2}$$

Here K is the thermal conductivity, ρ the resistivity, σ the Stefan-Boltzmann constant, e the emissivity of the sample, and T_0 the background temperature. In Eqs. (1) and (2), thermal emission from the two surfaces of the metal sample has been accounted for. From the experimental setup the temperature of the sample at the contact points of the electrode, which is approximately 3mm long, is much lower than the average temperature $< T >$. The temperature T_1 is about 400 K in the experiment. The ordinary differential equation (2) should describe the temperature distribution in the central part of the tungsten sample (which is about 7mm long) with the boundary conditions $T(x = 0) = T(x =$7mm$) = T_1$. The differential equation must be numerically solved. The following parameters are used: $\sigma = 5.67 \times 10^{-8}$[W/(m$^2 \cdot$ K^4)], $K(T) = 67.4 + 71.6e^{-T/2363.3} + 135.9e^{-T/268.3}$[W/(m $\cdot$ K)], which is simulated from the data in [89-94]. $\rho(T) = 3.22 \times 10^{-10}T + 7.71 \times 10^{-9}[\Omega \cdot \mathrm{m}]$, which is simulated from the experimental data for the temperature dependence of the resistivity. $e(T) = -0.0434 + 1.8524 \times 10^{-4}T + 1.954 \times 10^{-8}T^2$, which is simulated from the data in [25, 30-33]. $T_1 = 400$ K, and $T_0 = 300$ K.

Thus, in equation (2), we know all the parameters except the effective filling fraction f. Because of the CVD process in the fabrication of the photonic crystal, the tungsten rods in

the crystal are not completely filled. This, and the complex structure of the crystal makes it impossible to obtain an exact value for f from the experimental structure. To determine f, we assume various values for f, solve equation (2) numerically for the temperature distribution $T(x)$. Knowing $T(x)$, we can calculate the resistance of the sample to compare with experiment. For the different voltages V=3, 4, 5, 6.5 V, we obtain very similar values of f as 0.194, 0.196, 0.1925, 0.2015 respectively. Therefore, in our calculations, we fix f to be 0.196, which is the average.

The calculated temperature distributions at different electric currents as I=1.69, 2.04, 2.32, and 2.84 A using fixed f=0.196 are plotted in Figs. 5.4(a)-5.4(d), respectively. The experimental measured values of I are inserted into Eq. (2) as an input parameter. A significant feature of Fig. 5.4 is that in the central wide part (occupying more than one half) of the tungsten sample, the temperature is much higher (5-6 times higher) than that at the sample edge (the contact point of the electrode). The existence of hot regions in the tungsten sample and the strong inhomogeneous temperature distribution on a large space scale are evident. This is consistent with the experimental observation of the color of the metal sample at different regions. The corresponding average temperature of the whole sample is about 1173, 1313, 1413, and 1586 K. The apparent total resistance corresponding to these temperatures under our simple theoretical model is found to be 1.75, 1.96, 2.11, and 2.37 Ohm. Notice that both the average temperature and apparent resistance in the theory are very similar to the experimentally measured values, where $< T >$ is 1190, 1320, 1440, and 1535 K at the four input current values.

Now that we have obtained the temperature distribution function $T(x)$ across the tungsten sample, we can straightforwardly proceed to calculate the thermal radiation power spectrum from this metal lattice sample. The total radiation energy flux is obtained by summing up the contributions from different regions of the metal sample. The flux within a wavelength range in $\lambda - \lambda + d\lambda$ and a solid angle $d\Omega$ is given by Planck's law and Kirchhoff's law as

$$dj(\lambda) = \int_L \frac{2hc^2}{\lambda^5} \frac{(1/L)dx}{e^{hc/\lambda kT(x)} - 1} G(\lambda) d\lambda d\Omega. \tag{3}$$

Here the factor $1/L$ is due to the average over radiation from the whole tungsten sample. k is the Boltzmann constant, c the light speed in vacuum, and h Planck's constant. $G(\lambda)$ is the

emissivity of the tungsten sample, and it is equal to the absorptivity of the sample. Previous calculation results by means of an analytical modal solution approach and transfer-matrix method [81] showed that the absorption spectrum $G(\lambda)$ of the tungsten photonic crystal is sharply peaked between a wavelength range from 1.5 to 1.9 μm [15]. On the other hand, the thermal radiation spectrum from a blackbody at temperature $< T >$ is given by

$$dj_{bb}(\lambda) = \frac{2hc^2}{\lambda^5} \frac{1}{e^{hc/\lambda k < T >} - 1} d\lambda d\Omega. \tag{4}$$

The calculated thermal radiation spectra by means of Eq. (3) for these tungsten samples under different values of electric current I are shown in Fig. 5.5. For reference, we also plot the radiation spectra from a blackbody of the same average temperatures. Here we have included a solid angle of 2π in Eqs. (3) and (4) by considering thermal emission into the upper half space of the sample consistent with the experimental collection angle. The theoretical results clearly show that in the wavelength region of (about $1 - 3\mu m$), the radiation power exceeds by a factor of 3-4 those from blackbodies of the same average temperature, in agreement with experimental observations. While it is true that an object with a uniform temperature can never emit more power than a blackbody with the same temperature, a structured metal sample, having non-uniform temperature distributions, can emit more power than a blackbody with the same effective temperature. The maximum radiation power happens at wavelength $\lambda \approx 1.47\mu$m, and this value is determined by the sharp peak in the absorption spectrum of the photonic crystal. High-temperature objects have much stronger radiation power than low-temperature objects. Therefore, the hot wide central region of the tungsten lattice sample has an overwhelming effect on the thermal radiation spectrum, and lead to a radiation power several times larger than a blackbody of the same average temperatures.

In summary, we have utilized a simple model to examine recent experiments on thermal emission from metallic photonic crystals. We solve for the temperature distribution across the metallic lattice sample under Joule heating. The numerical simulations show that the central wide part of the sample has a much higher temperature than the edge parts. Due to the existence of a non-uniform temperature distribution, the thermal radiation power from the metal sample can significantly exceed those from a blackbody with the same average temperature.

This phenomenon is not in conflict with fundamental thermodynamical laws.

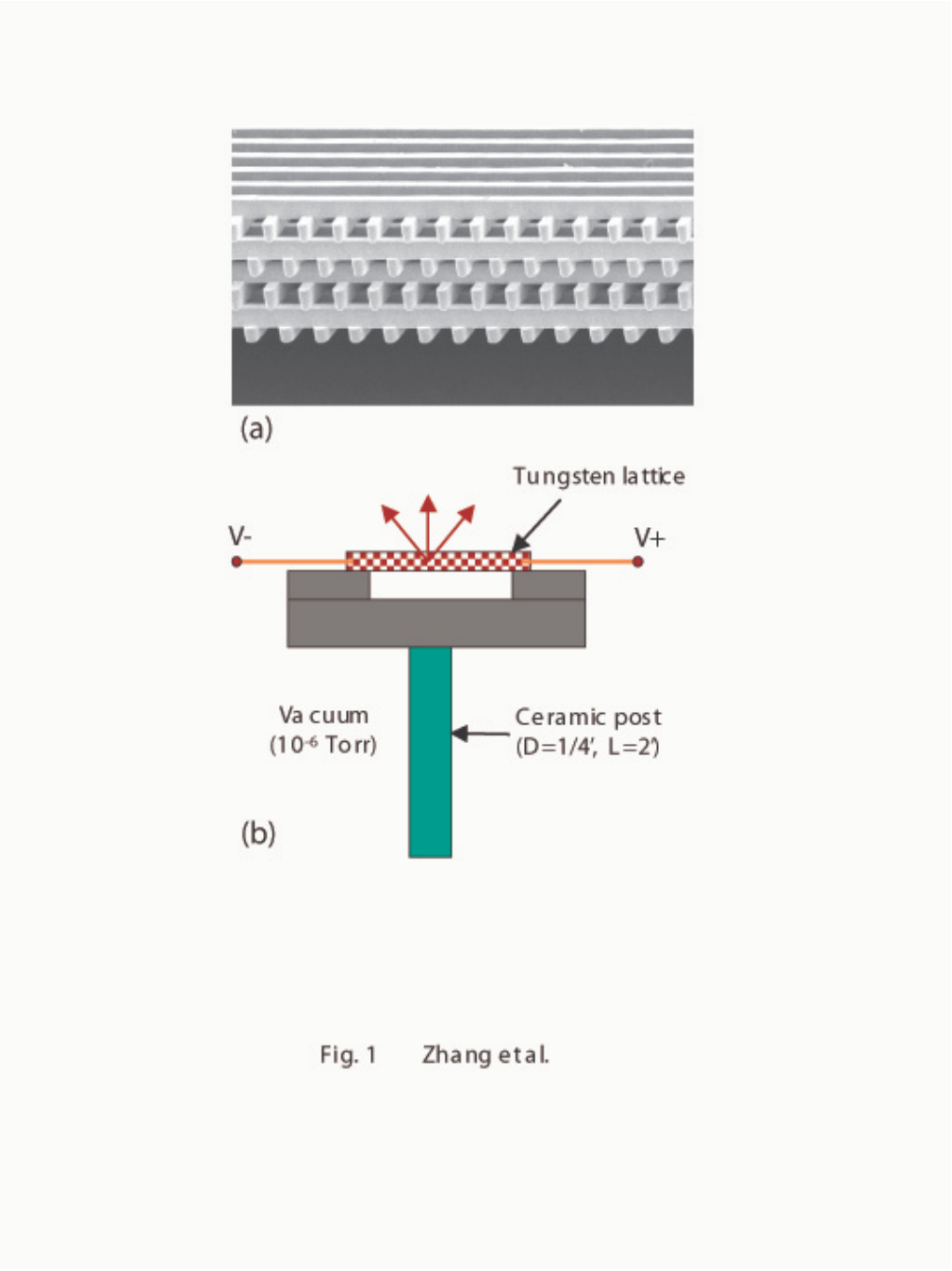

Figure 5.1 Experiment on thermal radiation from tungsten photonic crystal. (a) Scanning electron microscope picture of the 8-layer tungsten photonic crystal sample. Within each layer, the 1D rod width is 0.5 μm and the rod-to-rod spacing is 1.5 μm. (b) The schematic of the experimental setup for measuring the thermal radiation from the tungsten PC sample.

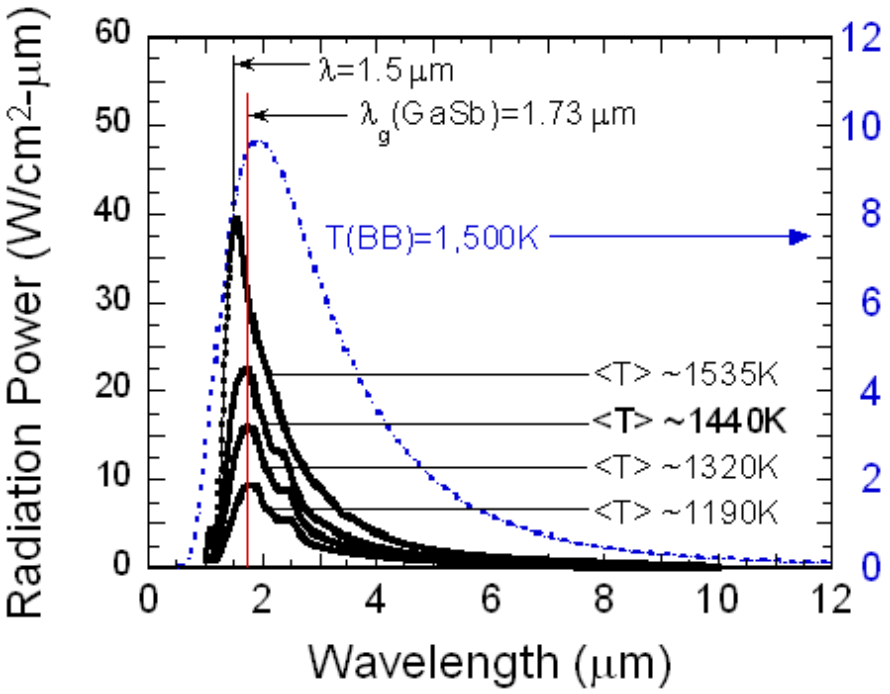

Figure 5.2 The measured emission power at different effective temperatures $< T >$. The dashed line is the blackbody radiation spectrum at 1500K.

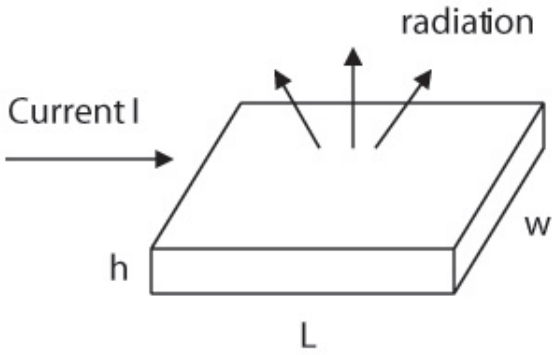

Fig. 3 Zhang et al

Figure 5.3 A simple model to acquire the temperature distribution of the tungsten sample. The PC slab is approximated as an effective homogeneous tungsten plate with length L, thickness h, and width w.

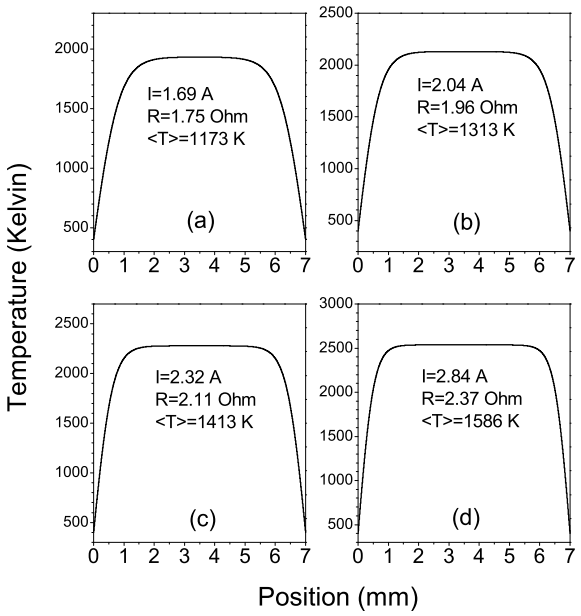

Fig. 4 Zhang et al.

Figure 5.4 Calculated temperature distribution at different electric current intensities. The corresponding apparent resistance and average sample temperature are also marked in the figures.

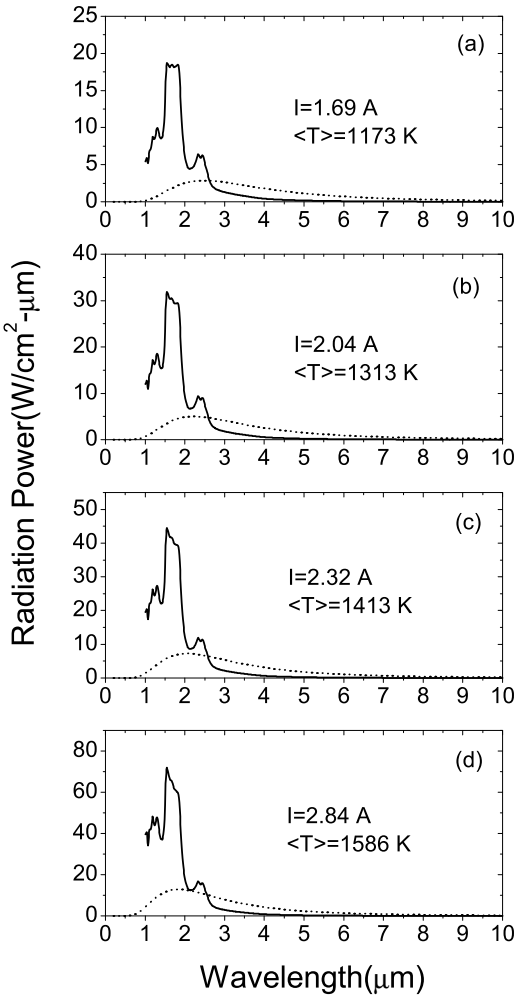

Fig. 5 Zhang et al.

Figure 5.5 Calculated thermal radiation power spectra at different electric current densities and average temperatures from the tungsten lattice sample (solid lines) and from a blackbody with the same average temperature (dashed lines).

APPENDIX ENVIRONMENT-DEPENDENT TIGHT-BINDING POTENTIAL MODELS

1 Fundamentals of tight-binding potential models

The expression for the binding energy of a system with M atoms and N valence electrons in tight-binding molecular dynamics is given by

$$E_{binding} = E_{bs} + E_{rep} - E_0. \tag{A.1}$$

The first term on the right hand side of Eq. (A.1) is the band structure energy which is equal to the sum of the one-electron eigenvalues ε_i of the occupied states given by a tight-binding Hamiltonian H_{TB},

$$E_{bs} = \sum_i f_i \varepsilon_i \tag{A.2}$$

where f_i is the electron occupation (Fermi-Dirac) function and $\sum_i f_i = N$.

The second term on the right hand side of Eq. (A.1) is a repulsive energy usually expressed as a sum of short-ranged pairwise interactions

$$E_{rep} = \frac{1}{2} \sum_{i,j} \phi(r_{i,j}) \tag{A.3}$$

or a functional of sum of pairwise interactions

$$E_{rep} = \sum_i F_i(\sum_j \phi(r_{i,j})) \tag{A.4}$$

where F is a function which for example can be a 4^{th} order polynomial (**?**).

The last term E_0 in Eq. (A.1) is a constant which represents the sum of the energies of the individual atoms.

2 Environment-Dependent tight-binding potential models

In the environment-dependent tight-binding potential model of Wang *et al.*, the minimal basis set is taken to be orthogonal. The effects of Löwdin orthogonality, three-center interactions and the variation of the local basis set with environment are taken into account empirically by renormalizing the interaction strength between atom pairs according to the surrounding atomic configurations. The TB hopping parameters and the repulsive interaction between atoms i and j depend on the environments of atoms i and j through two scaling functions (**?**). The first one is a screening function that is designed to weaken the interactions between two atoms when there are intervening atoms between them. Another is a bond-length scaling function which scales the interatomic distance (hence the interaction strength) between the two atoms according to their effective coordination numbers. Longer effective bond lengths are assumed for higher coordinated atoms.

Specifically, the hopping parameters and the pairwise repulsive potential for silicon and carbon are expressed as

$$h(r_{ij}) = \alpha_1 R_{ij}^{-\alpha_2} exp[-\alpha_3 R_{ij}^{\alpha_4}](1 - S_{ij}) \tag{A.5}$$

In this expression, $h(r_{ij})$ denotes the possible types of interatomic hopping parameters $h_{ss\sigma}$, $h_{sp\sigma}$, $h_{pp\sigma}$, $h_{pp\pi}$ and pairwise repulsive potential $\phi(r_{ij})$ between atoms i and j. r_{ij} is the real distance and R_{ij} is a scaled distance between atoms i and j. S_{ij} is a screening function. The parameters α_1, α_2, α_3, α_4, and parameters for the bond-length scaling function R_{ij} and the screening function S_{ij} can be different for different hopping parameters and the pairwise repulsive potential. Note that expression Eq. (A.5) will reduce to the traditional two-center form if we set $R_{ij} = r_{ij}$ and S_{ij}=0.

The screening function S_{ij} is expressed as a hyperbolic tangent (tanh) function (i.e., $S_{ij} = tanh(\xi_{ij})$) with argument ξ_{ij} given by

$$\xi_{ij} = \beta_1 \sum_l exp[-\beta_2 (\frac{r_{il} + r_{jl}}{r_{ij}})^{\beta_3}] \tag{A.6}$$

where β_1, β_2, and β_3 are adjustable parameters. Maximum screening effect occurs when the atom l is situated close to the line connecting the atoms i and j (i.e., $r_{il} + r_{lj}$ is minimum).

This approach allows us to distinguish between first and further neighbor interactions without explicit specification. This is well-suited for molecular dynamics simulations where it is difficult to define exactly which atoms are first neighbors and which are second neighbors.

The bond-length scaling function scales the distance between two atoms according to their effective coordination numbers. Longer effective bond lengths are assumed for higher coordinated atom pairs. leading to reduced interactions per atom pair for larger-coordinated structures. The scaling between the real and effective interatomic distance is given by

$$R_{ij} = r_{ij}(1 + \delta_1\Delta + \delta_2\Delta^2 + \delta_3\Delta^3) \tag{A.7}$$

where $\Delta = \frac{1}{2}[(\frac{n_i - n_0}{n_0}) + (\frac{n_j - n_0}{n_0})]$ is the fractional coordination number relative to the coordination number of the diamond structure n_0, averaged between atoms i and j. The coordination number can be modeled by a smooth function, $n_i = \sum_j (1 - S_{ij})$ with a proper choice of parameters for S_{ij} which has the form of the screening function described above.

Besides the hopping parameters, the diagonal matrix elements are also dependent on the bonding environments. The expression for the diagonal matrix elements is

$$e_{\lambda,i} = e_{\lambda,0} + \sum_j \Delta e_\lambda(r_{ij}) \tag{A.8}$$

where $\Delta e_\lambda(r_{ij})$ takes the same expression as Eq. (A.5), λ denotes the two types of orbitals (s or p). $e_{s,0}$ and $e_{p,0}$ are the on site energies of a free atom.

Finally, the repulsive energy term is expressed in a functional of the sum of pairwise interactions as defined in Eq. (A.4) in the previous section.

The parameters in the model are determined by fitting to the self-consistent first-principles density functional calculations results of electronic band structures and the cohesive energy versus volume curves of several crystalline structures of different coordination numbers.

For a silicon system, such crystalline structures include diamond, graphite, β-tin, simple cubic, bcc, and fcc structures. In addition, some elastic constants and vibration frequencies of the lowest-energy structures are also included in the fitting in order to ensure that the model gives good description of elastic and vibrational properties in addition to electronic structures and binding energies. The parameters of the EDTB Si potential are listed in Table A.1 and

Table A.2. The parameters for calculating the coordination number of Si are β_1 =2.0, β_2= 0.02895, β_3= 7.96284. The cutoff distance for the interaction is r_{ij} =5.2 Å.

Liu *et al.* (**?**) have extended the EDTB model to silver-silicon system. In their approach, the expression for the binding energy of a system is also given by Eq. (A.1). The same set of parameters used for band structure energy E_{bs} of pure silicon system are used for the silver-silicon system. The number of valence electron for silver atoms is set to be 1, whereas the number of valence electrons for silicon atoms is kept to be 4.

Finally, the repulsive energy term is expressed in a functional of sum of pairwise interactions as

$$E_{rep} = \sum_{i\in\alpha} F_i^{\alpha}(x_{i\in\alpha}) \qquad \alpha \in Si, Ag, \tag{A.9}$$

where $x_{i\in\alpha}$ is the sum of pairwise repulsive potential on atom i which is expressed as

$$x_{i\in\alpha} = \sum_{j\in\alpha} \phi_{\alpha-\alpha}(r_{ij}) + \kappa_{\alpha} \sum_{j\in\beta} \phi_{\alpha-\beta}(r_{ij}) \qquad \alpha,\beta \in Si, Ag \qquad \beta \neq \alpha, \tag{A.10}$$

where $\kappa_\alpha = 1.33$, if $\alpha \in$ Si and $\kappa_\alpha = 1.00$, if $\alpha \in$ Ag. The parameters of ϕ_{Si-Si} are the same as those for pure Si system which have been listed in Table A.1. The coefficients of the polynomial function F_i^{Si} is also taken from pure Si system which are listed in Table A.2.

The parameters of ϕ_{Ag-Ag}, ϕ_{Ag-Si}, and the coefficients of polynomial function for F_i^{Ag} listed in Table A.3 and A.4 are fitted to the cohesive energy versus volume curve of silver in the fcc structure and energy vs. Si-Ag bond distance curve of the tetrahedral $SiAg_4$ structure. These parameters and coefficients are further adjusted by fitting to the energy order of 8 selected models for Ag/Si(111) $\sqrt{3}\times\sqrt{3}$ phase (39).

	α_1	α_2	α_3	α_4	β_1	β_2	β_3
$h_{ss\sigma}$	-5.9974	0.4612	0.1040	2.3000	4.4864	0.1213	6.0817
$h_{sp\sigma}$	3.4834	0.0082	0.1146	1.8042	2.4750	0.1213	6.0817
$h_{pp\sigma}$	11.1023	0.7984	0.1800	1.4500	1.1360	0.1213	6.0817
$h_{pp\pi}$	-3.6014	1.3400	0.0500	2.2220	0.1000	0.1213	6.0817
ϕ	126.640	5.3600	0.7641	0.4536	37.00	0.56995	19.30
Δe_s, Δe_p	0.2830	0.1601	0.050686	2.1293	7.3076	0.07967	7.1364
	δ_1	δ_2	δ_3				
$h_{ss\sigma}$	0.0891	0.0494	-0.0252				
$h_{sp\sigma}$	0.1735	0.0494	-0.0252				
$h_{pp\sigma}$	0.0609	0.0494	-0.0252				
$h_{pp\pi}$	0.4671	0.0494	-0.0252				
ϕ	0.082661	-0.023572	0.006036				
Δe_s, Δe_p	0.7338	-0.03953	-0.062172				

Table A.1 The parameters obtained from the fitting for the EDTB model of Si (**?**). The α_1 is in the unit of eV. Other parameters are dimensionless.

	$c_0(eV)$	c_1	$c_2(eV^{-1})$	$c_3(eV^{-2})$	$c_4(eV^{-3})$
$x \geq 0.7$	-0.739×10^{-6}	0.96411	0.68061	-0.20893	0.02183
$x < 0.7$	-1.8664	6.3841	-3.3888	0.0	0.0

Table A.2 The coefficients of the polynomial function $f(x)$ for the EDTB potential of Si.

	α_1	α_2	α_3	α_4	β_1	β_2	β_3
ϕ_{Ag-Si}	89.3393	-4.68788	0.65683	0.87105	8.59	10.3793	11.269
ϕ_{Ag-Ag}	1085.1335	-7.46285	0.31731	1.38884	8.59	10.3793	11.269
	δ_1	δ_2	δ_3				
ϕ_{Ag-Si}	0.00	0.00	0.00				
ϕ_{Ag-Ag}	0.00	0.00	0.00				

Table A.3 The parameters used in the Ag-Si system. The parameters of the repulsive energy for Ag-Ag and Si-Ag are fitted and adjusted by Dr. Bei Liu. The α_1 is in the unit of eV. Other parameters are dimensionless.

	$c_0(eV)$	c_1	$c_2(eV^{-1})$	$c_3(eV^{-2})$	$c_4(eV^{-3})$
$x \geq 1.5$	-2.0445	0.7849	0.00	0.00	0.00
$0.2 \leq x < 1.5$	-3.6683	4.55378	-6.0909	5.02057	-1.4359
$x < 0.2$	-3.8553	23.249	-473.32	0.00	0.00

Table A.4 The coefficients of the polynomial function $f(x)$ for the EDTB potential of Ag.

BIBLIOGRAPHY

[1] L.T.Wille and J.Vennik, J.Phys. A **18**, L419 (1985).

[2] S.Kirkpatrick, Science **220**, 671 (1983)

[3] D.Vanderbilt, J.Comput. Phys. **56**, 259 (1984)

[4] J.H. Holland, Adaptation in Natural and Artificial Systems (The University of Michigan Press), Ann Arbor, (1975)

[5] P.Ballone and P.Milani, Phys.Rev. B **42**, 3201 (1990)

[6] D.E.Goldberg, Genetic Algorithm in Search, Optimization, and Machine Learning (Addison-Wesley), MA, (1989)

[7] R. Hornstra, Physica (Utrecht) **25**, 409 (1959).

[8] R.M.Grovenor, J.Phys.C **18**, 4079 (1985)

[9] T.A.Arias and J.D.Joannopoulos, Phys. Rev. B **49**, 4525 (1994).

[10] A.Maiti, M.F.Chisholm, S.J.Pennycook and S.T.Pantelides, Phys. Rev. Lett **77**, 1306 (1996)

[11] M.Kohyama, Phys. Status Solidi B **141**, 71, (1987)

[12] M.Kohyama, R.Yamamoto, Y.Ebata and M.Kinoshita, J.Phys.C 5, 3205, (1988)

[13] M.Kohyama, R.Yamamoto and M.Doyama, Phys. Status Solidi B **137**, 11, (1986)

[14] T.Paxton and A.P.Sutton, J.Phys.C **21**, L481 (1988)

[15] A.Levi, D.A.Smith and J.T.Weizel, J.Appl.Phys. **69**, 2048, (1991)

[16] A.P.Sutton and V.Vitek, Philos.Trans.R.Soc.London Ser.A **309**, 71, (1987)

[17] O.A.Shenderova , D.W.Brenner and L.H.Yang, Phys. Rev. B **60**, 7043, (1999)

[18] J.R.Morris, Z.Y.Lu, D.M.Ring, J.B.Xiang, K.M.Ho, C.Z.Wang and C.L.Fu, Phys Rev. B **58**, 11241, (1998)

[19] D.M.Deaven and K.M.Ho, Phys Rev. Lette **75**, 288, (1995)

[20] A.R.Oganov and C.W.Glass **124**, 244704, (2006)

[21] F.C.Chuang, C.Z.Wang and K.H.Ho Phys. Rev. B **73**, 125431, (2006)

[22] F.C.Chuang, C.V.Ciobanu, V.B.Shenoy, C.Z.Wang and K.M.Ho, Surface Science **573**, L375, (2004)

[23] F.C.Chuang, C.V.Ciobanu, C.Predescu, C.Z.Wang and K.M.Ho, Surface Science **578**, 183, (2005)

[24] T.L.Chan, C.V.Ciobanu, F.C.Chaung, N.Lu, C.Z.Wang and K.M.Ho, Nano Lette, **6**,277, (2006)

[25] J.L.Rouviere, A.Bourret, in Polycrystalline Semiconductors (Ref.6), p.19

[26] J.L.Rouviere, A.Bourret, J.Phys.(Paris) **51**, Cl-329, (1990)

[27] M.F.Chisholm, S.J.Pennycook, MRS Bull. **22**, 53, (1997)

[28] M.S.Tang, C.Z.Wang, C.T.Chan and K.M.Ho, Phys.Rev.B **53**,979, (1996)

[29] K. J. Wan, X. F. Lin, and J. Nogami, Phy. Rev. B. **47** 13700, (1993).

[30] T. Fukuda, Phy. Rev. B **50** 1969 (1994).

[31] Steven C. Erwin, Phys. Rev. Lett. **75** 1973 (1995).

[32] S. C. Erwin and Hanno H. Weitering, Phy. Rev. Lett. **81** 2296 (1998).

[33] L. Lottermoser, E. Landemark, D.-M. Smilgies, M. Nielsen, R. Feidenhans'l, G. Falkenberg, R. L. Johnson, M. Gierer, A. P. Seitsonen, H. Kleine, H. Bludau, H. Over, S. K. Kim, and F. Jona, Phy. Rev. Lett. **81** 3980 (1998).

[34] C. Collazo-Davila, D. Grozea, and L. D. Marks, Phy. Rev. Lett. **80**, 1678 (1998).

[35] M. Gurnett, J. B. Gustafsson, K. O. Magnusson, S. M. Widstrand, and L. S. O. Johansson, Phy. Rev. B **66** 161101 (2002).

[36] R. J. Wilson and S. Chiang, Phys. Rev. Lett. **58**, 369 (1987).

[37] T. L. Porter, C. S. Chang, and I. S. T. Tsong, Phys. Rev. Lett. **60**, 1739 (1988).

[38] E. Vlieg, A. W. Denier, Van Der Gon, J. F. Van Der Veen, J. E. MacDonald, and C. Norris, Surf. Sci. **209**, 100 (1989).

[39] Y. G. Ding, C. T. Chan, and K. M. Ho, Phys. Rev. Lett. **67**, 1454 (1991).

[40] A. Shibata, Y. Kimura, and K. Takayanagi, Surf. Sci. **275**, L697 (1992).

[41] E. J. van Loenen, J. E. Demuth, R. M. Tromp, and R. J. Hamers, Phy. Rev. Lett. **58** 373 (1994).

[42] H. Tajiri, K. Sumitani, S. Nakatani, A. Nojima, T. Takahashi, K. Akimoto, H. Sugiyama, X. Zhang, and H. Kawata, Phys. Rev. B **68**, 035330 (2003).

[43] Iwao Matsuda, Harumo Morikawa, Canhua Liu, Satoru Ohuchi, Shuji Hasegawa, Taichi Okuda, Toyohiko Kinoshita, Carlo Ottaviani, Antonio Cricenti, Marie D'angelo, Patrick Soukiassian, and Guy Le Lay, Phy. Rev. B. **68**, 85407 (2003).

[44] H. Lipson and K. E. Singer, J. Phys. C **7**, 12 (1974).

[45] G. LeLay and J. P. Faurie, Surf. Sci. **69**, 295 (1977).

[46] H. E. Bishop and J. C. Riviere, Br. J. Appl. Phys. **2**, 1635 (1969).

[47] A. A. Baski, J. Nogami, and C. F. Quate, Phys. Rev. B 41, **10** 247 (1990).

[48] J. D. O'Mahony, C. H. Patterson, J. F. McGilp, F. M. Leibsle, P. Weightman, and C. F. J. Flipse, Surf. Sci. **277**, L57 (1992).

[49] J. D. O'Mahony, J. F. McGilp, C. F. J. Flipse, P. Weightman, and F. M. Leibsle, Phys. Rev. B **49**, 2527 (1994).

[50] C. Schamper, W. Moritz, H. Schulz, R. Feidenhans'l, M. Nielsen, F. Grey, and R. L. Johnson, Phys. Rev. B **43**, 12 130 (1991).

[51] J. R. Power, P. Weightman, and J. D. O'Mahony, Phys. Rev. B **56**, 3587 (1997).

[52] I. R. Collins, J. T. Moran, P. T. Andrews, R. Cosso, J. D. O'Mahony, J. F. McGilp, and G. Margaritondo, Surf. Sci. **325**, 45 (1995).

[53] K. N. Altmann, J. N. Crain, A. Kirakosian, J.-L. Lin, D. Y. Petrovykh, F. J. Himpsel, and R. Losio, Phys. Rev. B **64**, 035406 (2001).

[54] I. G. Hill and A. B. McLean, Appl. Surf. Sci. **123**, 371 (1998).

[55] H. M. Zhang, T. Balasubramanian, and R. I. G. Uhrberg, Phys. Rev. B **65**, 035314 (2002).

[56] R. Losio, K. N. Altmann, and F. J. Himpsel, Phys. Rev. Lett. **85**, 808 (2000).

[57] L. D. Marks and R. Plass, Phys. Rev. Lett. **75**, 2172 (1995).

[58] T. Hasegawa, S. Hosaka, and S. Hosoki, Surf. Sci. **357**, 858 (1996).

[59] M.-H. Kang and J. Y. Lee, Surf. Sci. **531**, 1 (2003).

[60] S. C. Erwin, Phys. Rev. Lett. **91**, 206101 (2003).

[61] H. S. Yoon, S. J. Park, J. E. Lee, C. N. Whang, and I.-W. Lyo, Phys. Rev. Lett. **92**, 096801 (2004).

[62] E. Yablonovitch, Phys. Rev. Lett. **58**, 2059 (1987).

[63] J. D. Joannopoulos, R. D. Meade, and J. N. Winn, *Photonic Crystals* (Princeton University Press, Princeton, NJ, 1995).

[64] S. Y. Lin, J. G. Fleming, D. L. Hetherington, B. K. Smith, R. Biswas, K. M. Ho, M. M. Sigalas, W. Zurbrzycki, S. R. Kurtz, and J. Bur, Nature (London) **394**, 251 (1998).

[65] S. Y. Lin, J. G. Fleming, E.Chow, J. Bur, K. K. Choi, and A. Goldberg, Phys. Rev. B **62**, R2243 (2000).

[66] J. C. Knight, T. A. Birks, P. S. J. Russell, and D. M. Atkin, Opt. Lett. **21**, 1547 (1996).

[67] M. Notomi, Phys. Rev. B **62**, 10696 (2000).

[68] E. R. Brown and O. B. MacMahon, Appl. Phys. Lett. **67**, 2138 (1995).

[69] D. F. Sievenpiper, M. E. Sickmiller, and E. Yablonovitch, Phys. Rev. Lett. **76**, 2480 (1996).

[70] S. Gupta, G. Tuttle, M. Sigalas, and K. M. Ho, Appl. Phys. Lett. **71**, 2412 (1997).

[71] M. J. Bloemer and M. Scalora, Appl. Phys. Lett. **72**, 1676 (1998).

[72] A. Moroz, Phys. Rev. Lett. **83**, 5274 (1999).

[73] W. Y. Zhang, X. Y. Lei, Z. L. Wang, D. G. Zheng, W. Y. Tam, C. T. Chan, and P. Sheng, Phys. Rev. Lett. **84**, 2853 (2000).

[74] J. G. Fleming, S. Y. Lin, I. El-Kady, R. Biswas, and K. M. Ho, Nature **417**, 52 (2002).

[75] S. Y. Lin, J. G. Fleming, and I. El-Kady, Opt. Lett. **28**, 1909 (2003).

[76] S. Y. Lin, J. Moreno, and J. G. Fleming, Appl. Phys. Lett. **83**, 380 (2003).

[77] S. Y. Lin, J. G. Fleming, and I. El-Kady, Appl. Phys. Lett. **83**, 593 (2003).

[78] Z. Y. Li and K. M. Ho, Phys. Rev. B **67**, 165104 (2003).

[79] Z. Y. Li, I. El-Kady, K. M. Ho, S. Y. Lin, and J. G. Fleming, J. Appl. Phys. **93**, 38 (2003).

[80] S. Y. Lin, J. G. Fleming, Z. Y. Li, I. El-Kady, R. Biswas, and K. M. Ho, J. Opt. Soc. Am. B **20**, 1538 (2003).

[81] Z. Y. Li, Phys. Rev. B **66**, 241103(R) (2002).

[82] T. Trupke, P. Würfel, and M. A. Green, Appl. Phys. Lett. **84**, 1997 (2004).

[83] S. Y. Lin, J. Moreno, and J. G. Fleming, Appl. Phys. Lett. **84**, 1999 (2003).

[84] C. Luo, A. Narayanaswamy, G. Chen, and J. D. Joannopoulos, Phys. Rev. Lett. **93**, 213905 (2004).

[85] "Report on the Mechanical and Thermal Properties of Tungsten and TZM Sheet Produced in the Refractory Metal Sheet Rolling Program," Southern Research Institute Report 7563-1479-XII to the U.S. Bureau of Naval Weapons, August 31, (1966).

[86] "Tungsten Technical Brochure," Metallwerk Plansee, Reute, Austria, (1985).

[87] Y. S. Touloukian *et al.*, Thermophysical Properties of Matter, Volume 1, IFI/Plenum Publishing, New York, 428 (1970).

[88] V. A. Sorkin, Tungsten Technical Data, Technical report of VNIITS, Moscow, **84**, (1988).

[89] C. R. Tipton, editor, Reactor Handbook, Volume I, Interscience Publishers, Inc. New York, 672 (1960).

[90] D. T. Hurd,"Tungsten," Metals Handbook, Volume 1, Properties and Selection of Metals, American Society for Metals, Metals Park, Novelty, 1227 (1961).

[91] W. E. Forsythe and A. G. Worthing,"The Properties of Tungsten and the Characteristics of Tungsten Lamps," The Astrophysical Journal, University of Chicago Press, Volume LXI, 146 (1924).

[92] Y. S. Touloukian and D. P. DeWitt, "Thermal Radiative Properties of Metallic Elements and Alloys," Thermophysical Properties of Matter, Volume 7, IFI/Plenum Publishing, New York, 776 (1970).

[93] D. E. Gray, American Institute of Physics Handbook, New York, 6 (1972).

[94] I. K. Kikoin, Tables of Physical Values Handbook, Moscow, Atomizdat, 107 (1976).